

Entanglement renormalization and gauge symmetry

L. Tagliacozzo and G. Vidal

School of Mathematics and Physics, University of Queensland, QLD 4072, Australia

(Received 2 August 2010; revised manuscript received 7 January 2011; published 16 March 2011)

A lattice gauge theory is described by a redundantly large vector space that is subject to local constraints and can be regarded as the low-energy limit of an extended lattice model with a local symmetry. We propose a numerical coarse-graining scheme to produce low-energy, effective descriptions of lattice models with a local symmetry such that the local symmetry is exactly preserved during coarse-graining. Our approach results in a variational ansatz for the ground state(s) and low-energy excitations of such models and, by extension, of lattice gauge theories. This ansatz incorporates the local symmetry in its structure and exploits it to obtain a significant reduction of computational costs. We test the approach in the context of a Z_2 lattice gauge theory formulated as the low-energy theory of a specific regime of the toric code with a magnetic field, for lattices with up to 16×16 sites ($16^2 \times 2 = 512$ spins) on a torus. We reproduce the well-known ground-state phase diagram of the model, consisting of a deconfined and spin-polarized phases separated by a continuous quantum phase transition, and obtain accurate estimates of energy gaps, ground-state fidelities, Wilson loops, and several other quantities.

DOI: [10.1103/PhysRevB.83.115127](https://doi.org/10.1103/PhysRevB.83.115127)

PACS number(s): 03.65.Vf, 03.65.Ta, 12.40.Nn, 11.15.Ha

I. INTRODUCTION

Gauge invariance is one of the most important concepts in modern physics. It is at the core of the equivalence principle of general relativity¹ as well as an essential ingredient in the quantum-field formulation of the standard model of particle physics.² More broadly, gauge theories are useful in several research areas, including condensed matter and nuclear and high-energy physics.

Wilson's lattice gauge theory³ was proposed in order to study quantum chromodynamics (QCD) nonperturbatively. By replacing continuous space-time by a discrete lattice, it offers both a specific regularization scheme and a convenient starting point for numerical studies. Through large-scale Monte Carlo computations, lattice gauge theory has provided, among other results, numerical evidence of QCD confinement⁴ and of the presence of a chiral condensate,⁵ the determination from first principles of the value of the quark masses,⁶ and numerical evidences of the formation of quark-gluon plasma at high temperatures.⁷ In spite of their incontestable importance in lattice gauge theory calculations, Monte Carlo sampling techniques cannot be applied to systems with large chemical potential due to the fermionic sign problem. It is therefore desirable to explore alternative approaches.

In the past few years, tensor network algorithms have received increasing attention as variational, nonperturbative methods to study spin lattice systems. The simplest tensor network variational ansatz, the matrix product state^{8–10} (MPS), is the basis of White's extremely successful density matrix renormalization group^{11–13} (DMRG) algorithm to compute the ground state of spin chains. Several generalizations of the MPS to two and larger spatial dimensions exist both for spin and fermionic systems, such as the projected entangled-pair states^{14–28} (PEPS), also referred to as tensor product states, and the multiscale entanglement renormalization ansatz^{29–37} (MERA), both of which lead to scalable simulations. Since tensor network algorithms do not suffer from the sign problem, they are suitable to study problems beyond the reach of Monte Carlo techniques. Recent calculations include frustrated

antiferromagnets^{19,35,38} and interacting fermions^{24,39} in two spatial dimensions.

The goal of this article is to explore the use of tensor network techniques within the Hamiltonian formulation of lattice gauge theory. We will consider the simplest nontrivial case, namely Z_2 lattice gauge theory in two spatial dimensions,^{3,40–42} with a Hamiltonian that contains the usual kinetic and potential terms for the gauge field and no fermionic matter. The ground-state phase diagram of the theory, which we aim to reproduce, is already well understood, due, e.g., to previous studies using Monte Carlo techniques. Therefore the aim of the present article is not to uncover new physics but rather to describe a new approach and to confirm its validity in a well-known, simple context. The merit of the present strategy resides in that it can be generalized to more complex settings beyond the reach of Monte Carlo techniques.

In this work we will describe (i) a coarse-graining scheme for the lattice model specifically designed to preserve and exploit its local Z_2 symmetry, (ii) a variational ansatz for the ground state(s) and low-energy states of theory, and (iii) numerical results to illustrate the potential of the approach. We will regard lattice gauge theories from the broader and more recent perspective of topological order.⁴³ The Z_2 lattice gauge theory can be studied as the low-energy sector of a spin model, namely Kitaev's toric code model,⁴⁴ in a suitable limit (see also Refs. 45–48). The hopping term of the gauge field is implemented by deforming the toric code with a magnetic field, as investigated in Refs. 49 and 50. In the deformed toric code model, the Z_2 group is a local symmetry of the spin Hamiltonian, and states are not forced to be gauge invariant. In particular, excited states exist that are gauge covariant. Such states can be understood as describing the presence of static matter in specific locations of the lattice. Our variational ansatz can also represent such states.

A. Previous work

Previous related work can be divided into two categories. On the one hand, Sugihara⁵¹ has investigated the use of a

MPS to describe the ground state of Z_2 lattice gauge theory in quasi-one-dimensional systems, both directly or through a mapping to the quantum Ising model. We notice that no attempt is made to adapt the MPS, primarily a tensor network for one-dimensional systems (where Z_2 lattice gauge theory is trivial) to the presence of the symmetry.

On the other hand, Schuch, Cirac, and Perez-Garcia,⁵² as well as Swingle and Wen,⁵³ have recently considered a PEPS representation of a state of a two dimensional lattice with topological order and have investigated how to extract topological information from it, while Chen *et al.*⁵⁴ have stressed the importance of explicitly preserving certain symmetry in a PEPS in order to represent topological order. In contrast with the present work, where we propose and benchmark an algorithm to compute the ground state(s) of a two-dimensional system with topological order (in some limiting regime) or, relatedly, of Z_2 lattice gauge theory, none of these previous contributions explains how to actually obtain, given a Hamiltonian of a topologically ordered system, a tensor network representation of its ground state(s).

B. Guide

The article is organized in several sections. Sections II–IV are entirely devoted to introducing background material, whereas Sec. V describes the proposed approach. Section VI presents benchmark results, and Sec. VII concludes with a discussion of the proposed technique and of a number of possible generalizations to be pursued in future work.

In more detail, Sec. II reviews the toric code and its magnetic field deformation, Sec. III reviews two-dimensional Z_2 lattice gauge theory and its duality with the two-dimensional quantum Ising model, and Sec. IV contains a short introduction to coarse-graining transformations based on entanglement renormalization and to the MERA. A reader with sufficient previous knowledge on the toric code, Z_2 lattice gauge theory, and entanglement renormalization may decide to skip Secs. II–IV in a first reading and jump directly to Sec. V, which describes our proposal—possibly returning to Secs. II–IV to seek clarification on nomenclature. A reader who simply wants to obtain an overall picture of the approach may prefer to read the *summary* below and then have a look at the benchmark results of Sec. VI.

C. Summary

As explained in Sec. V, the lattice model is coarse grained by means of a transformation that breaks into two parts, W_{exact} and W_{num} . The first part W_{exact} can be viewed as a local version of the duality transformation to the quantum Ising model. The spin model is divided into blocks of spins, and within each block a duality transformation to the Ising model is implemented. This produces two types of spins: at the boundary between blocks, spins which have not yet been mapped to the Ising model (referred to as *constrained* spins) and, in the interior of each block, spins that have been mapped to the Ising model (referred to as *free* spins). The second part W_{num} of the coarse-graining transformation replaces the free spins inside a block with a single, effective *free* spin.

The resulting effective spin model contains *constrained* spins interspersed with *free* spins.

Importantly, the local Z_2 symmetry, which acts on the constrained spins only, is *exactly preserved* during the coarse-graining. In addition, thanks to applying duality mappings to the Ising model only within each block of spins, the coarse-graining transformation is completely *local*: Any local operator of the original model is mapped into a local operator of the effective model. Finally, composition of coarse-graining transformations reduces a finite system to a small number of spins, which can be addressed with exact diagonalization. As is customary in tensor network algorithms, a *variational ansatz* for, e.g., the ground state of the model is then obtained by regarding the coefficients that characterize the coarse-graining transformation as variational parameters.

Thus, one of the highlights of the approach is that it produces a tensor network representation of the wave function of the ground state (and low-energy states) of the model, from which the expectation value of arbitrary local observables can be computed. We note here that, depending on the choice of transformation W_{num} , namely depending on whether W_{num} incorporates *disentangles*, our approach can consider arbitrarily large systems or is restricted to small lattices. In the first case, one can study the renormalization group flow to a fixed point (in preparation). In the second case, on which we will concentrate here in addition to local observables one can also evaluate nonlocal order parameters, Wilson loops and ground-state fidelities, see Sec. VI.

As is customary in most tensor network algorithms, entanglement is central to the present discussion. The more entangled a system is, the more costly it is to simulate it with a tensor network ansatz. An important aspect of our work is that it highlights the potential role of duality transformations in transforming a strongly entangled ground state into a weakly entangled one, which is then suitable for tensor network algorithms. In particular, the toric code for small magnetic field has a robustly entangled ground state that is mapped into an Ising model with large magnetic field, whose ground state is only weakly entangled; see Fig. 1. A key of our approach is then to be able to map the model to its less entangled dual while preserving locality. This is precisely the role of W_{exact} . After the entanglement in the ground state has been reduced significantly, as illustrated in Fig. 1, W_{num} can proceed to coarse-grain the system by discarding high-energy degrees of freedom. The reduction of entanglement obtained with W_{exact} significantly decreases computational costs. As a result, with a fixed computational cost (as parameterized by some refinement parameter χ ; see Sec. VI), use of W_{exact} produces an improvement of four orders of magnitude in the estimate of the ground-state energy in a 4×4 lattice, as shown in Fig 2. As a side remark the entanglement structure of the same lattice gauge theory we consider here has also been studied in Ref. 58.

II. THE DEFORMED TORIC CODE

In this section we briefly review the toric code model, an exactly solvable model proposed by Kitaev in Ref. 44. We also review a deformation of the toric code model obtained by adding a magnetic field on the \hat{x} direction, as analyzed

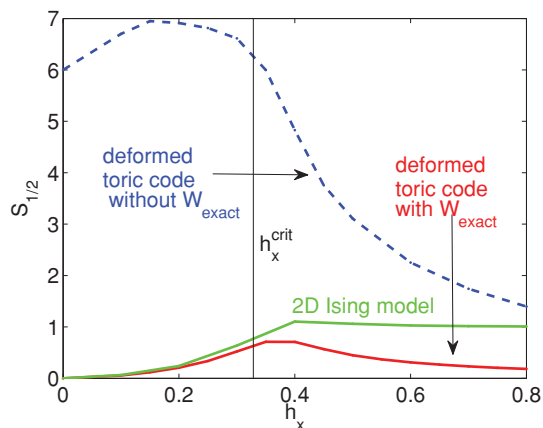


FIG. 1. (Color online) Entanglement entropy of half a 4×4 (32 spin) lattice \mathcal{L} in the ground state $|\Phi_{+,+}\rangle$ of H_{TC}^x as a function of the magnetic field h_x . The critical magnetic field $h_x^{\text{crit}} = 0.3285(1)$ ⁵⁵ is denoted by a vertical line. The blue (top) curve is a lower bound to the entanglement entropy of the deformed toric code model without W_{exact} . For comparison, the green (middle) curve corresponds to the entanglement entropy of the ground state of the quantum Ising model on a 4×4 (16 spin) lattice with periodic boundary conditions and no vacancy. Finally, the red (bottom) curve corresponds to the entanglement left in the ground state of H_{TC}^x after applying the analytical transformation W_{exact} . Note that the amount of entanglement is very similar to that of the Ising model. Similar reduction of the entanglement entropy was observed by several authors in the context of global symmetries.^{56,57} Thus, by implementing a local version of the duality transformation to the Ising model, the analytical transformation W_{exact} maps the robustly entangled ground state $|\Phi_{+,+}\rangle$ of the deformed toric code model to a significantly less entangled ground state.

by Trebst *et al.* in Ref. 49 and by Hamma *et al.* in Ref. 50, for which an exact solution no longer exists. The deformed toric code model has a local Z_2 symmetry and will be used throughout this work to illustrate the proposed coarse-graining transformation.

A. Toric code

We consider the toric code model⁴⁴ on a square lattice \mathcal{L} made of $L \times L$ sites and with periodic boundary conditions. Recall that in this model a spin-1/2 degree of freedom sits on each of the $2L^2$ links of the lattice, with total vector space

$$\mathbb{V}_{\text{TC}} \cong (\mathbb{C}_2)^{\otimes 2L^2} \quad (1)$$

and Hamiltonian

$$H_{\text{TC}} \equiv -J_e \sum_s A_s - J_m \sum_p B_p, \quad (2)$$

with $J_e, J_m > 0$. Here the star operator $A_s = \prod_{j \in s} \sigma_j^x$ acts on the spins adjacent to site s and the plaquette operator $B_p = \prod_{j \in p} \sigma_j^z$ acts on all the spins surrounding plaquette p , where σ^x and σ^z are Pauli matrices; see Fig. 3.

1. Ground states and topological sectors

All operators A_s and B_p commute with each other and the ground-state subspace of Hamiltonian H_{TC} consists of the

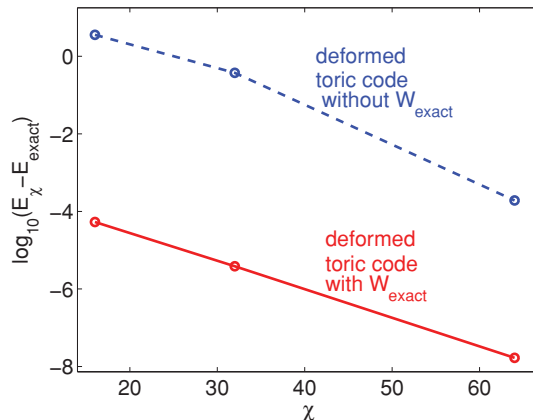


FIG. 2. (Color online) Accuracy in the ground-state energy of the deformed toric code in a 4×4 lattice, as a function of the refinement parameter χ (see Sec. VI), for magnetic field $h_x = 0.1$ in H_{TC}^x of Eq. (11). On the 4×4 lattice we obtain the exact ground-state energy by directly diagonalizing the full Hamiltonian and use it to assess the precision of the results as a function of the computational cost. The computational cost grows monotonically with χ . Both curves correspond to using a tree tensor network (see Sec. V) as a means to numerically coarse-grain the system. However, the lower curve was obtained by first applying W_{exact} (in this work we refer as the *hybrid ansatz* to the combination of W_{exact} and a tree tensor network, see Sec. V). For a fixed value of χ , which roughly corresponds to the same computational cost, the hybrid ansatz leads to about four more digits of accuracy in the ground-state energy.

states $|\xi\rangle \in \mathbb{V}_{\text{TC}}$ that simultaneously fulfill the *star constraints*

$$A_s |\xi\rangle = |\xi\rangle, \quad \forall s \in \mathcal{L}, \quad (3)$$

as well as the *plaquette constraints*

$$B_p |\xi\rangle = |\xi\rangle, \quad \forall p \in \mathcal{L}, \quad (4)$$

and thus have energy $-L^2(J_e + J_m)$. Note that, on the torus, there are L^2 star operators A_s and L^2 plaquette operators B_p

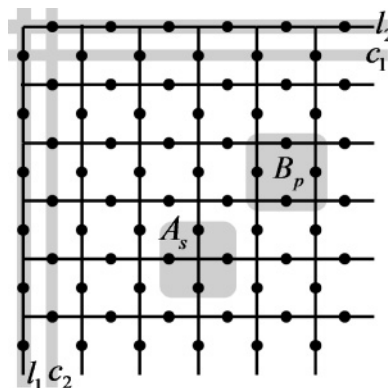


FIG. 3. In the toric code model, spin-1/2 degrees of freedom sit at the edges of a square lattice \mathcal{L} . Here we consider a lattice \mathcal{L} , with periodic boundary conditions on both directions (torus). A star operator A_s acts on the four spins surrounding site $s \in \mathcal{L}$, whereas a plaquette operator B_p acts on the four spins surrounding a plaquette p . The noncontractible cuts c_1 and c_2 and the noncontractible loops l_1 and l_2 are the support of operators X_1 and X_2 in Eq. (6) and of operators Z_1 and Z_2 in Eq. (8), respectively.

fulfilling

$$\prod_{s \in \mathcal{L}} A_s = \mathbf{I}, \quad \prod_{p \in \mathcal{L}} B_p = \mathbf{I}. \quad (5)$$

Therefore, Eqs. (3) and (4) only represent $L^2 - 1$ independent constraints each, that is, a total of $2L^2 - 2$ constraints in the space of $2L^2$ spin-1/2 sites. As a result, there are $2^2 = 4$ linearly independent ground states. Let us introduce the operators

$$X_1 \equiv \prod_{j \in c_1} \sigma_j^x, \quad X_2 \equiv \prod_{j \in c_2} \sigma_j^x, \quad (6)$$

where c_1 and c_2 denote the two noncontractible cuts of Fig. 3. Operators X_1 and X_2 commute with each other and with H_{TC} and cannot be expressed as products of A_s 's and B_p 's. The eigenvectors $|\Phi_{v_1, v_2}\rangle$ of X_1 and X_2 ,

$$X_1 |\Phi_{v_1, v_2}\rangle = v_1 |\Phi_{v_1, v_2}\rangle, \quad X_2 |\Phi_{v_1, v_2}\rangle = v_2 |\Phi_{v_1, v_2}\rangle, \quad (7)$$

where $v_1, v_2 = \pm 1$, form a basis of the ground-state subspace. We refer to $\{|\Phi_{+,+}\rangle, |\Phi_{+,-}\rangle, |\Phi_{-,+}\rangle, |\Phi_{-,-}\rangle\}$ as the ground states of the four *topological sectors* of the model, and we label each topological sector by the pair (v_1, v_2) .

For later reference, we also introduce two operators

$$Z_1 \equiv \prod_{j \in l_1} \sigma_j^z, \quad Z_2 \equiv \prod_{j \in l_2} \sigma_j^z, \quad (8)$$

where l_1 and l_2 denote the two noncontractible loops of Fig. 3.

2. Electric charges and magnetic vortices

Excited states of the toric code Hamiltonian H_{TC} are characterized by violations of the star and plaquette constraints, Eqs. (3) and (4). We say that state $|\xi\rangle$ contains an *electric charge* on site s if $A_s |\xi\rangle = -|\xi\rangle$. Similarly, we say that state $|\xi\rangle$ contains a *magnetic vortex* (or magnetic monopole) in plaquette p if $B_p |\xi\rangle = -|\xi\rangle$.

Operator σ_j^z acting on a ground state $|\Phi_{v_1, v_2}\rangle$ produces an excited state with a pair of electric charges sitting on the two sites s and r connected by link j . Indeed, since for site s (equivalently, for site r) we have $A_s \sigma_j^z = -\sigma_j^z A_s$, it follows that

$$A_s (\sigma_j^z |\Phi_{v_1, v_2}\rangle) = -\sigma_j^z A_s |\Phi_{v_1, v_2}\rangle = -(\sigma_j^z |\Phi_{v_1, v_2}\rangle). \quad (9)$$

State $\sigma_j^z |\Phi_{v_1, v_2}\rangle$ has an energy $4J_e$ above the ground-state energy, since each violation of a star constraint increases the energy by $2J_e$. More generally, any other state that fulfills Eqs. (3) and (4) except in two sites, again corresponding to the presence of two electric charges, has energy $4J_e$ above the ground state. This implies that a pair of electric charges created locally by acting with σ_j^z on the ground state can be separated in space without a change in energy. We say that electric charges are *deconfined*. On the other hand, operator σ_j^x acting on a ground state $|\Phi_{v_1, v_2}\rangle$ produces a pair of magnetic vortices (monopoles) sitting on the two plaquettes p and q that contain link j . For plaquette p (equivalently, for plaquette q) we have $B_p \sigma_j^x = -\sigma_j^x B_p$ and therefore

$$B_p (\sigma_j^x |\Phi_{v_1, v_2}\rangle) = -\sigma_j^x B_p |\Phi_{v_1, v_2}\rangle = -(\sigma_j^x |\Phi_{v_1, v_2}\rangle). \quad (10)$$

State $\sigma_j^x |\Phi_{v_1, v_2}\rangle$ has an energy $4J_m$ above the ground-state energy. Any other state with just two magnetic vortices

has energy $4J_m$ and we say that magnetic vortices are also *deconfined*.

B. Hamiltonian deformation of the toric code

The toric code Hamiltonian H_{TC} in Eq. (2) is exactly solvable. Here we will be interested in a nonsolvable deformation of the toric code obtained by introducing a magnetic field in the \hat{x} direction,^{49,50}

$$H_{\text{TC}}^x \equiv -J_e \sum_s A_s - J_m \sum_p B_p - h_x \sum_j \sigma_j^x. \quad (11)$$

The magnetic field lifts the ground-state degeneracy. Notice, however, that since $\sum_j \sigma_j^x$ also commutes with the operators X_1 and X_2 , Hamiltonian H_{TC}^x still decomposes into four sectors (v_1, v_2) . The ground state of any of the sectors may no longer fulfill the plaquette constraints, indicating the presence of pairs of magnetic vortices, for which $\sum_j \sigma_j^x$ also acts as a hopping term.

The limit $J_e \gg J_m, h_x$, where low-energy states fulfill the star constraints of Eq. (3) and therefore contain no electric charges, is well understood⁴⁹ (it corresponds to the Z_2 lattice gauge theory,⁴² which in turn is dual to the quantum Ising model, as reviewed in Sec. III). In this regime, the ground-state phase diagram of H_{TC}^x contains two phases, one in which pairs of magnetic vortices are deconfined and another with a Bose condensate of magnetic vortices.

1. Deconfined phase

For small values of the magnetic field h_x , $h_x \ll 1$, the model is in a *deconfined phase*, in which a pair of (dressed) magnetic vortices created locally can be separated an arbitrary distance incurring only a finite energy penalty. [Notice that in this work the term *deconfined* refers to magnetic vortices, and not to the electric charges, which by construction are not present in the low-energy sector of the model.]

The deconfined phase is a topologically ordered phase with four nearly degenerate ground states on the torus, one for each sector (v_1, v_2) . The sector $(+, +)$ has the smallest energy and the energy separation Δ to another sector vanishes exponentially fast with the linear size L of the lattice,⁴⁴

$$\Delta \approx e^{-L/\xi}, \quad (12)$$

where ξ is a finite length scale that vanishes for $h_x = 0$, i.e., $\Delta = 0$ for the undeformed toric code.

To further characterize this phase, let us introduce the string operator^{42,59-61}

$$X_3 \equiv \prod_{j \in c_3} \sigma_j^x, \quad (13)$$

where c_3 is the cut of Fig. 4 connecting a pair (p_0, p_1) of plaquettes that are as distant as possible in the torus. Since X_3 anticommutes with B_{p_0} and B_{p_1} , and commutes with the rest of plaquette terms, an argument similar to that in Eq. (10) above shows that this operator acting on a ground state $|\Phi_{v_1, v_2}\rangle$ for $h_x = 0$ (undeformed toric code) produces a state with a pair of magnetic vortices/monopoles sitting on plaquettes p_0 and p_1 . This state is orthogonal to the ground state and therefore, for

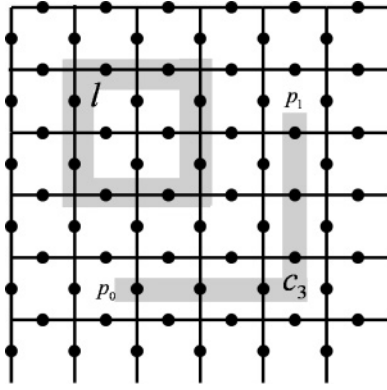


FIG. 4. Cut c_3 connects two plaquettes p_0 and p_1 that are as far apart in \mathcal{L} as possible. Example of loop l that has a length of eight spins, $|l| = 8$, and encloses an area of four plaquettes, $\Sigma(l) = 4$.

$h_x = 0$, the ground-state expectation value of X_3 vanishes,

$$\langle X_3 \rangle = 0. \quad (14)$$

In the thermodynamic (or large L) limit, $\langle X_3 \rangle$ vanishes for the whole deconfined phase and it is used as a (nonlocal) disorder parameter.

Alternatively, the deconfined phase can also be characterized by the scaling of the expectation value of Wilson loops.³ For every contractible loop l on \mathcal{L} (see Fig. 4) we can define a *Wilson loop operator* $Z[l]$ by

$$Z[l] \equiv \prod_{j \in l} \sigma_j^z. \quad (15)$$

Operator $Z[l]$ amounts to the product of operators B_p for all plaquettes p contained in the interior of loop l . Therefore, for any ground state $|\Phi_{v_1, v_2}\rangle$ for $h_x = 0$ (undeformed toric code), we have the expectation value

$$\langle Z[l] \rangle = 1. \quad (16)$$

More generally, in the deconfined phase Wilson loops obey a *perimeter law*,³ in the sense that they decay as

$$\langle Z[l] \rangle \approx e^{-\alpha p(l)}, \quad (17)$$

where $p(l)$ is the length of the loop l , and where $\alpha \geq 0$ vanishes for $h_x = 0$, recovering Eq. (16) for the undeformed toric code. The behavior of the Wilson loop with respect to its length is related to the dependence of the potential between two static electric charges with their mutual distance, which is in turn induced by their interaction with the gauge fields. In the deconfined phase this potential is such that the force between the two charges does not increase with their distance. This translate into a decay of the Wilson loop proportional to the perimeter of the loop, as can be found in standard textbooks about lattice gauge theories⁶² and in the original papers on the subject.^{3,63-65}

2. Spin-polarized phase

For large values of h_x , the model is in a state where the spins are polarized in the x direction.

This phase has a unique global ground state, corresponding to the ground state of sector $(+, +)$, and the energy separation

to the other sectors grows linearly in the system size L ,

$$\Delta \approx L. \quad (18)$$

The spin-polarized phase can be interpreted as a Bose condensate of magnetic vortices/monopoles and is characterized by a nonvanishing [actually, positive] value of the (nonlocal) order parameter $\langle X_3 \rangle$,

$$\langle X_3 \rangle \neq 0, \quad (19)$$

which can be interpreted as the square of the expectation value of a creation operator for a single magnetic vortex (see Sec. III D), with $\langle X_3 \rangle = 1$ for the completely polarized state at $h_x \rightarrow \infty$. Alternatively, it is characterized by an *area law* of the ground-state expectation value of Wilson loops,

$$\langle Z[l] \rangle \approx e^{-\beta a(l)}, \quad (20)$$

where $a(l)$ is the area enclosed by the loop l , and where $\beta = \infty$ for $h_x \rightarrow \infty$, in which case $\langle Z[l] \rangle = 0$.

3. Continuous quantum phase transition

For an intermediate value of h_x of about $h_x = 0.3285$,⁵⁵ the system undergoes a continuous quantum phase transition. This is in the same universality class of that of the 2D quantum Ising model (see Sec. III D) or the 3D classical Ising model, but it is special in that it separates two phases which cannot be distinguished by a local order parameter. Instead, the transition can be characterized by the nonlocal order parameter $\langle X_3 \rangle$, which detects the formation of a Bose condensate of magnetic vortices/monopoles, or by the scaling of Wilson loops as a function of their size and by the presence/absence of an approximate ground-state degeneracy.

C. Local symmetry

The symmetries of the deformed toric code Hamiltonian H_{TC}^x in Eq. (11) play a central role in this article. Apart from the $Z_2 \times Z_2$ symmetry generated by operators X_1 and X_2 , H_{TC}^x is also invariant under unitary conjugation by any star operator A_s ,

$$A_s H_{\text{TC}}^x A_s^\dagger = H_{\text{TC}}^x, \quad \forall s \in \mathcal{L}, \quad (21)$$

which follows from recalling that $[H_{\text{TC}}^x, A_s] = 0$ and from noticing that $A_s = A_s^\dagger = A_s^{-1}$. Therefore, the deformed toric code Hamiltonian H_{TC}^x has a *local* Z_2 symmetry, generated by unitary transformations of the form

$$A_s : \mathbb{V}_{\text{TC}} \rightarrow \mathbb{V}_{\text{TC}}, \quad (A_s)^2 = \mathbb{I}, \quad (22)$$

which simultaneously flip the four spins included in a star s for any choice of star $s \in \mathcal{L}$.

This local symmetry implies the presence of $L^2 - 1$ constants of motion, namely the eigenvalues ± 1 of $L^2 - 1$ independent star operators A_s . In particular, a state that fulfills all the star constraints of Eq. (3), $A_s |\xi\rangle = |\xi\rangle$, that is, a state that is invariant under the local symmetry remains so under a time evolution generated by H_{TC}^x . It is important to note, however, that the vector space \mathbb{V}_{TC} also contains states that are not invariant under A_s . For instance, we have already seen that a state with a pair of electric charges, Eq. (9), violates the star constraint in two sites, where it transforms as $A_s |\xi\rangle = -|\xi\rangle$.

D. Entanglement

Entanglement is another aspect of the deformed toric code model that will play a key role in for subsequent discussions on how to coarse-grain the system.

When the lattice is in a pure state $|\Psi\rangle \in \mathbb{V}_{\mathcal{L}}$, the entanglement between a block of spins and the rest of the system can be measured by means of the Von Neumann entropy S of the reduced density matrix ρ of the block of spins, known as *entanglement entropy*,

$$S = -\text{tr}(\rho \log_2 \rho), \quad \rho \equiv \text{tr}_{\text{rest}}|\Psi\rangle\langle\Psi|. \quad (23)$$

Figure 1 shows the entanglement entropy of a block of four spins as a function of the magnetic field h_x , when the system is in the ground state $|\Phi_{+,+}\rangle$ of H_{TC}^x . Note that for $h_x = 0$, corresponding to the (undeformed) toric code, the entanglement entropy of the block is significantly large, indicating that the ground state is very entangled. This is in sharp contrast with the entanglement entropy for large h_x , which tends to zero. In this second case, each spin is completely polarized in the \hat{x} direction and the ground state is a product, unentangled state.

III. Z_2 LATTICE GAUGE THEORY AND THE QUANTUM ISING MODEL

In this section we briefly review Z_2 lattice gauge theory^{3,40,42,66–68} in two spatial dimensions and its connection to the two-dimensional quantum Ising model.^{42,69,70} We also introduce a convenient graphical notation for the different Hamiltonian terms in the Hamiltonian, and pieces of the stabilizer formalism, including the transformation rules of Pauli matrices under so-called controlled-NOT CNOT gates. The stabilizer formalism provides us with the natural language to describe the coarse-graining transformation of systems with a local symmetry, as described in Sec. V.

A. Z_2 lattice gauge theory

The considered restriction $J_e \gg J_m, h_x$ on H_{TC}^x ensures that low-energy states fulfill the star constraints of Eq. (3). If, instead, we impose those constraints by truncating the vector space of the model, we are left with the vector space $\mathbb{V}_{\text{LGT}} \subseteq \mathbb{V}_{\text{TC}}$ of Z_2 lattice gauge theory,^{3,40,42}

$$\mathbb{V}_{\text{LGT}} \equiv \{|\xi\rangle \in \mathbb{V}_{\text{TC}} : A_s|\xi\rangle = |\xi\rangle \forall s \in \mathcal{L}\} \quad (24)$$

$$\cong (\mathbb{C}_2)^{\otimes L^2+1}. \quad (25)$$

When projected onto \mathbb{V}_{LGT} , the Hamiltonian H_{TC}^x in Eq. (11) becomes

$$H_{\text{LGT}} = -\sum_p B_p - h_x \sum_j \sigma_j^x, \quad (26)$$

where we have neglected a constant term $-L^2 J_e$ and we have set for simplicity, without loss of generality, $J_m = 1$. It is also understood that each term in H_{LGT} is projected onto \mathbb{V}_{LGT} . This model has been extensively studied before.^{40,42,67,68} It was originally introduced as a model that presents two different phases that cannot be distinguished with a local order parameter. By increasing the intensity of the magnetic field one can indeed drive a transition from the deconfined phase

(at small magnetic fields) to a spin-polarized phase (at large magnetic field). The phase transition around $h_x \simeq 0.3$ is in the 3D Ising model universality class. The Z_2 lattice gauge theory has also been intensively studied because it presents the ideal testing ground for new ideas, since its relative simplicity (as compared to gauge theories with larger gauge groups) allows us to obtain very precise numerical results in Monte Carlo simulations.⁶⁸ Further interest in the model comes from a conjecture that relates its critical properties with the ones of the finite temperature deconfining transition of an $\text{SU}(2)$ lattice gauge theory in $3+1$ dimensions.⁷¹ Finally, the existence of a duality transformation between the Z_2 lattice gauge theory and the quantum 2D Ising model, as we review in Sec. III D, has inspired a lot of work in finding the relevant order parameter for confinement.⁷²

By construction, the Z_2 lattice gauge can be regarded as a low-energy, effective model of H_{TC}^x (for $J_e \gg J_m, h_x$) and therefore has the same ground-state phase diagram. The Hamiltonian H_{LGT} has a $Z_2 \times Z_2$ symmetry corresponding to operators X_1 and X_2 (properly projected onto \mathbb{V}_{LGT}). However, it is worth emphasizing that, in contrast with Hamiltonian H_{TC}^x , Hamiltonian H_{LGT} does not have a local symmetry. Indeed, H_{LGT} is defined on the subspace $\mathbb{V}_{\text{LGT}} \subseteq \mathbb{V}_{\text{TC}}$ of Eq. (24), which is made of vectors that fulfill the star constraints. That is, each star operator A_s acts as the identity operator in \mathbb{V}_{LGT} , and therefore the assertion that H_{LGT} is invariant under transformation A_s is an empty statement.

The present work aims at developing a coarse-graining scheme for lattice models with a local symmetry. For concreteness, we will most of the time restrict our attention to the subspace of states that fulfill the symmetry constraints, that is, \mathbb{V}_{LGT} . In this case, the coarse-graining transformation can be used also to obtain a low-energy, effective description of lattice gauge models, as illustrated here in the context of Z_2 lattice gauge theory.

B. Graphical representation of Hamiltonians

In this article we will represent star and plaquette operators graphically by just drawing the corresponding lattice. For instance, Fig. 5(i) represents the toric code Hamiltonian H_{TC} of Eq. (2). The toric code Hamiltonian H_{TC} can be defined on a more general lattice by considering star operators A_s and

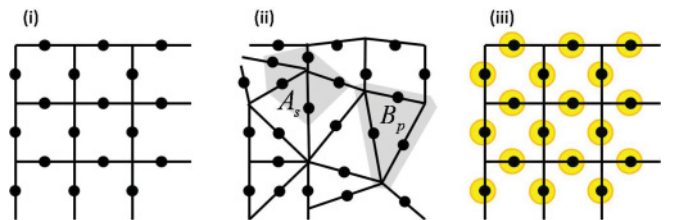


FIG. 5. (Color online) (i) Graphical representation of the Hamiltonian H_{TC} for a 3×3 lattice \mathcal{L} . A four-spin star operator A_s acts on each site $s \in \mathcal{L}$, and a four-spin plaquette operator B_p acts on each plaquette $p \in \mathcal{L}$. (ii) Hamiltonian H_{TC} can also be defined on more general lattices. The example shows an irregular lattice with a five-spin star operator A_s and a three-spin plaquette operator B_p . (iii) Additionally, we represent the magnetic field of the deformed toric code Hamiltonian H_{TC}^x by means of a yellow shade surrounding each qubit on which $-h_x \sigma^x$ acts.

plaquette operators B_p that involve a variable number of spins or qubits; see Fig. 5(ii). In that case, we will also often just denote H_{TC} by drawing the underlying lattice.

In addition, the presence of a magnetic field or, more generally, of related additional interactions, will be represented by a yellow shaded region enclosing all relevant qubits. For instance, Fig. 5(iii) represents the deformed toric code Hamiltonian H_{TC}^x of Eq. (11).

C. Qubits and CNOTs

In order to describe our coarse-graining scheme for the deformed toric code model and the Z_2 lattice gauge theory, it is convenient to introduce first some basic pieces of nomenclature and formalism frequently used in the area of quantum information.

A spin-1/2 degree of freedom is an example of a quantum bit or *qubit*. We will work with two preferred basis of a qubit. One basis corresponds to the eigenvectors $|0\rangle$ and $|1\rangle$ of σ^z and the second one to the eigenvectors $|+\rangle$ and $|-\rangle$ of σ^x ,

$$\sigma^z|0\rangle = |0\rangle, \quad \sigma^x|+\rangle = |+\rangle, \quad (27)$$

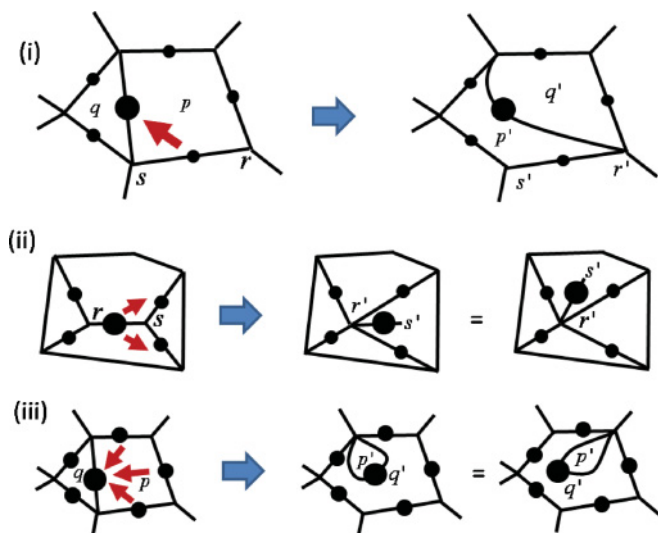


FIG. 6. (Color online) (i) A CNOT is represented with an arrow from the control qubit to the target qubit. When applied on two adjacent qubits, it reconnects the target qubit. This affects the two stars r, s to which the control qubits belongs, which become r' and s' , as well as the two plaquettes p, q to which the target qubit belongs, which become p' and q' . (ii) A sequence of CNOTs can also be used to focus a star operator A_s on a single qubit, on which it acts as $A_{s'} = \sigma_s^x$. As a result, the neighboring site r increases the number of qubits connected to it, becoming r' . Note that the single-qubit star can be represented inside any of the plaquettes surrounding site r' . In this work we restrict our attention to the subspace of states that are invariant under star constraints, Eq. (3). The single-qubit star $A_{s'}$ forces the qubit to be in state $|+\rangle$ and therefore unentangled with respect to the rest of the qubits. We will use this fact to remove it from the effective description of the system at low energies. (iii) A sequence of CNOTs can be used to focus a plaquette operator B_p on a single qubit, on which it acts as $B_{p'} = \sigma_{p'}^z$. As a result, the neighboring plaquette q expands to q' . Note that the single-qubit plaquette can be represented as connected to *any* of the sites of plaquette q' .

$$\sigma^z|1\rangle = -|1\rangle, \quad \sigma^x|-\rangle = -|-\rangle, \quad (28)$$

where

$$|+\rangle = \frac{|0\rangle + |1\rangle}{\sqrt{2}}, \quad |-\rangle = \frac{|0\rangle - |1\rangle}{\sqrt{2}}. \quad (29)$$

A CNOT gate is a unitary transformation U_{CNOT} on two qubits given by

$$U_{\text{CNOT}} \equiv |0\rangle\langle 0| \otimes \mathbf{I} + |1\rangle\langle 1| \otimes \sigma^x \quad (30)$$

$$= \mathbf{I} \otimes |+\rangle\langle +| + \sigma^z \otimes |-\rangle\langle -|, \quad (31)$$

where the first and second qubits are referred to as the *control* and *target* qubits, respectively. We use the stabilizer formalism⁷³ to study how operators evolve under the application of a CNOT gate. Specifically, under conjugation by a CNOT, Pauli matrices on the control and target qubits are transformed according to

$$\mathbf{I} \otimes \sigma^z \leftrightarrow \sigma^z \otimes \sigma^z, \quad \sigma^z \otimes \mathbf{I} \leftrightarrow \sigma^z \otimes \mathbf{I}, \quad (32)$$

$$\mathbf{I} \otimes \sigma^x \leftrightarrow \mathbf{I} \otimes \sigma^x, \quad \sigma^x \otimes \mathbf{I} \leftrightarrow \sigma^x \otimes \sigma^x. \quad (33)$$

Given the toric code Hamiltonian on a given lattice, the action of a CNOT between two neighboring qubits is to reconnect the target qubit according to Fig. 6(i). Note that we represent a CNOT gate by an arrow from the control qubit to the target qubit.

Following Ref. 74, a sequence of CNOTs involving the qubits of a star can be used to reduce the star operator to a single qubit; Fig. 6(ii). The star operator reduces to σ^x acting on that qubit. Similarly, a sequence of CNOTs involving the qubits of a plaquette can then be used to reduce the plaquette to a single qubit, as illustrated in Fig. 6(iii). The plaquette operator reduces to σ^z acting on that qubit.

Of course, a CNOT between two qubits will not only modify the star and plaquette operators. For instance, according to Eq. (33), a magnetic field σ^x acting on the control qubit will be transformed into a $\sigma^x \otimes \sigma^x$ interaction between control and target qubits; see Fig. 7. In the rest of the article we refer to qubits as spins.

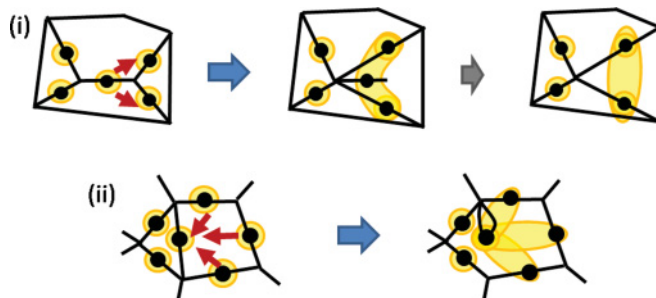


FIG. 7. (Color online) The magnetic field σ^x acting on control qubits expands into a multi-qubit interaction $\sigma^x \otimes \sigma^x \otimes \dots$ including all target qubits. (i) In concentrating a star operator on a single qubit, the magnetic field on that qubit spreads to all the qubits originally involved on that star. In the subspace of locally symmetric states, Eq. (3), we can remove the control qubit (now in state $|+\rangle$) and thus unentangled from the rest of the system, see caption of Fig 6(ii) from the effective description. (ii) In concentrating a plaquette operator on a single qubit, the magnetic field σ^x of the rest of qubits on the original plaquette turn into a $\sigma^x \otimes \sigma_x$ interaction between those qubits and the target qubit.

D. Duality transformation: quantum Ising model

The Z_2 lattice gauge theory has plaquette degrees of freedom that can take two values, namely the eigenvalues ± 1 of the plaquette operators B_p , corresponding to the absence/presence of a magnetic vortex on that plaquette. Thus plaquettes behave as spin-1/2 degree of freedom. In addition, as argued in Eq. (10), the operator σ_j^x can flip the value of the two nearest neighbor plaquettes p and q that share the link j . This interpretation of the Z_2 lattice gauge theory as a spin model can be materialized explicitly by means of a well-known duality transformation that maps it into the quantum Ising model with a transverse magnetic field⁴² (see Appendix A),

$$H_{\text{Ising}} \equiv -h_x \sum_{\langle p,p' \rangle} \mu_p^x \mu_{p'}^x - \sum_p \mu_p^z, \quad (34)$$

where the spins are placed on the sites of a $L \times L$ lattice $\mathcal{L}^{\text{dual}}$ dual to the original lattice \mathcal{L} (i.e., they can be identified with the plaquettes of \mathcal{L}) and μ^x and μ^z are Pauli matrices; see Figs. 8–9. However, the resulting Ising model inherits two unconventional elements. On the one hand, lattice $\mathcal{L}^{\text{dual}}$ has one vacancy, i.e., there are only $L^2 - 1$ spins, reflecting the fact that the Z_2 lattice gauge theory only had $L^2 - 1$ independent plaquettes. (It is worth noting that the μ_p^x terms around the vacancy explicitly break the Z_2 symmetry of the Ising model.) On the other hand, there are two additional *nonlocal* spin-1/2 degrees of freedom, associated to operators X_1 and X_2 , each of which is coupled to L spins along one of the two directions in $\mathcal{L}^{\text{dual}}$; see Fig. 9.

By ignoring the presence of the vacancy and nonlocal spins, which do not affect local observables in the thermodynamic limit, the ground-state phase diagram of H_{LGT} (and thus of H_{TC}^x for $J_e \gg J_m, h_x$) can be recovered from the well-known ground-state phase diagram of H_{Ising} ^{15,32,55,75–78} by inverting the duality transformation. Recall that the 2D quantum Ising model at zero temperature has a disordered phase for small h_x and an ordered phase for large h_x , as characterized by the vanishing (respectively nonvanishing) value of the

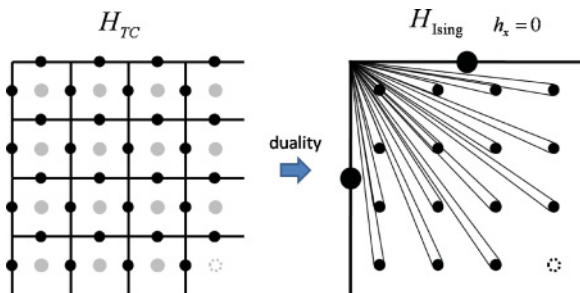


FIG. 8. (Color online) (i) (Left) Graphical representation of the toric code Hamiltonian H_{TC} , equivalently, H_{LGT} for $h_x = 0$, for a lattice \mathcal{L} made of 4×4 sites or $4^2 \times 2 = 16$ spins. (Right) Graphical representation of the dual quantum Ising Hamiltonian H_{Ising} . There are $4 \times 4 - 1 = 15$ spins with a single-spin plaquette operator, that is, with a transverse magnetic field $-J_m \mu^z$. Notice the vacancy and two additional *topological* spins which are not subject to any star or plaquette constraints. Operators X_1 and X_2 act each on one of these qubits.

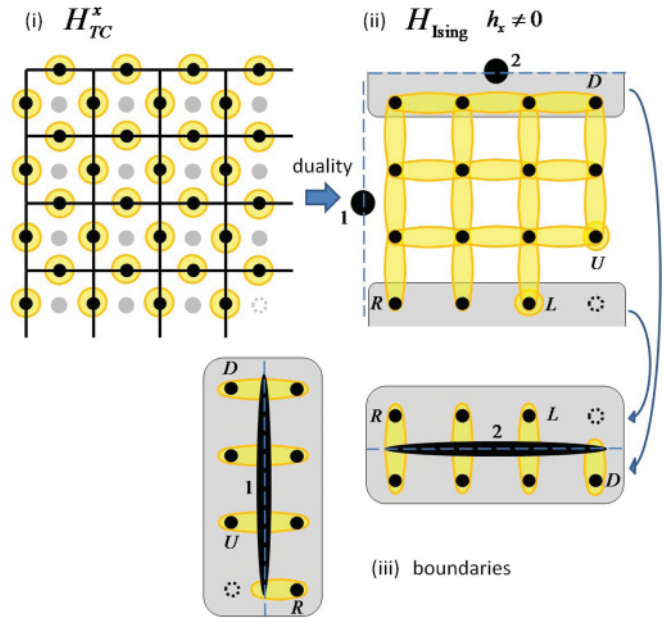


FIG. 9. (Color online) (i) Graphical representation of the Hamiltonian H_{TC}^x , equivalently H_{LGT} , including the magnetic field $-h_x \sum_j \sigma_j^x$. (ii) The duality transformation maps the magnetic field to a nearest-neighbor ferromagnetic Ising interaction $-h_x \mu^x \otimes \mu^x$. For simplicity, transverse magnetic field terms $-J_m \mu^z$ of H_{Ising} are not depicted here. Note that the four spins surrounding the vacancy, denoted U , D , L , and R , as well as all boundary spins, follow a different interaction pattern. On the one hand, U and L have one interaction term less than the rest of the spins but have instead an additional term $-h_x \mu^x$ acting on them. (iii) On the other hand, the nearest-neighbor interaction between spins p and q at both sides of a boundary is mediated by a coupling $-h_x \mu_p^x \otimes X_\alpha \otimes \mu_q^x$ that includes one topological spin [here, X_α corresponds to one of the nonlocal operators X_1 or X_2 defined in Eq. (6)]. In the sector $(+, +)$, the topological spins are in state $|+\rangle \otimes |+\rangle$ and boundary spins are coupled with a regular Ising interaction $-h_x \mu_p^x \otimes \mu_q^x$, corresponding to periodic boundary conditions (BC) in both directions. However, in, e.g., sector $(+, -)$ the topological spins are in state $|+\rangle \otimes |-\rangle$ and the coupling between the spins in the uppermost and lowermost rows becomes antiferromagnetic, $h_x \mu_p^x \otimes \mu_q^x$, corresponding to antiperiodic BC in the vertical direction, while in the horizontal direction the BC are still periodic. In general, sector (v_1, v_2) the BC in the horizontal (respectively vertical) direction will be periodic/antiperiodic depending on whether v_1 (respectively v_2) is $+/-$.

spontaneous magnetization m_x ,

$$m_x \equiv \frac{1}{L^2} \sum_p \langle \mu_p^x \rangle, \quad (35)$$

which is a local order parameter, and that the two phases are separated by a continuous quantum phase transition that occurs, indeed, at $h_x \approx 0.33$.^{15,32,55,75–78}

In particular, we can gain insight into the meaning of the nonlocal order parameter $\langle X_3 \rangle$ of the deformed toric code by noting that operator X_3 in Eq. (13) can be written as

$$X_3 = \mu_{p_0}^x \mu_{p_1}^x, \quad (36)$$

where p_0 and p_1 are two spins in $\mathcal{L}^{\text{dual}}$ (or plaquettes in \mathcal{L}) separated by $O(L)$ sites. In the limit $L \gg 1$ of a large lattice,

where $\langle \mu_{p_0}^x \mu_{p_1}^x \rangle$ is expected to factorize into $\langle \mu_{p_0}^x \rangle \langle \mu_{p_1}^x \rangle$ since plaquettes p_0 and p_1 are far apart, this expectation value equals the square of the spontaneous magnetization m_x ,

$$\langle X_3 \rangle = \langle \mu_{p_0}^x \mu_{p_1}^x \rangle \approx \langle \mu_{p_0}^x \rangle \langle \mu_{p_1}^x \rangle = m_x^2 \quad (37)$$

Thus, we can interpret $\langle X_3 \rangle$ as the square of the expectation value of a (fictitious) creation operator of *single* magnetic vortices, and interpret a vanishing/nonvanishing value for $\langle X_3 \rangle$ as indicating the absence/presence of a Bose condensate of magnetic vortices.

IV. ENTANGLEMENT RENORMALIZATION

In this section we briefly review one possible route to coarse-graining a lattice model in real space based on entanglement renormalization.^{29,30,33,79} Entanglement renormalization is a specific real-space implementation of the renormalization group.⁸⁰ The coarse-graining transformation can be used to define the MERA,³⁰ a variational ansatz for ground states and low-energy states of a local Hamiltonian. We also review how to use entanglement renormalization and the MERA in the presence of a global internal symmetry in such a way that the symmetry is exactly preserved and exploited to reduce computational costs. Then, in Sec. V, we will explore how to generalize entanglement renormalization and the MERA in the presence of a local symmetry.

A. Coarse-graining transformation

Given a lattice model, characterized by a lattice \mathcal{L} and a Hamiltonian H , a coarse-graining transformation aims to produce a new, simplified lattice model, characterized by a coarse-grained lattice \mathcal{L}' with fewer sites and an effective Hamiltonian H' . Here we are interested in a coarse-graining transformation W

$$W^\dagger : \mathbb{V}_{\mathcal{L}} \rightarrow \mathbb{V}_{\mathcal{L}'} \quad (38)$$

that defines a linear map from the space $\mathbb{V}_{\mathcal{L}}$ of the original model to the space $\mathbb{V}_{\mathcal{L}'}$ of the effective model; see Fig. 10(i). [Note that, for consistency with Ref. 30, we actually regard W as a map from $\mathbb{V}_{\mathcal{L}'} to $\mathbb{V}_{\mathcal{L}}$.]$

More specifically, we consider a coarse-graining transformation W that maps local operators in \mathcal{L} (that is operators that act nontrivially on a finite subset of neighboring sites of \mathcal{L}) into local operators in \mathcal{L}' . This property is automatically fulfilled if W is an isometric tensor,

$$W^\dagger W = I_{\mathcal{L}}, \quad (39)$$

that decomposes as the product of isometric tensors u and w ; see Figs. 10(ii)–9(iii),

$$u^\dagger u = I, \quad w^\dagger w = I, \quad (40)$$

known as *disentangler*s and *isometries*, which corresponds to one step of *entanglement renormalization*.²⁹ Indeed, as shown in Fig. 11, in this case local operators are mapped into local operators. In particular, if the Hamiltonian H of the original lattice model decomposes as the sum of local terms, then the effective Hamiltonian H' , depicted in Fig. 12, will also decompose as a sum of local terms.

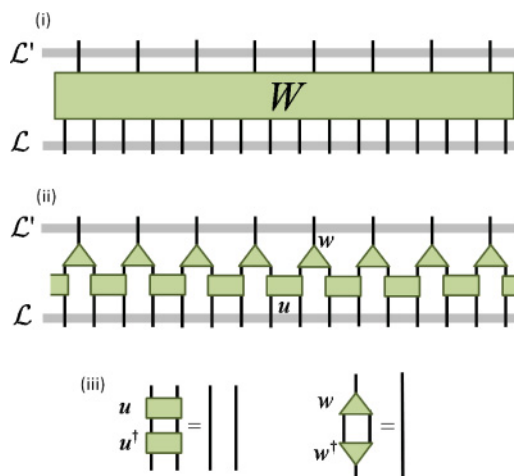


FIG. 10. (Color online) (i) The coarse-graining transformation W defines a linear map between the space $\mathbb{V}_{\mathcal{L}'}$ of lattice \mathcal{L}' and the space $\mathbb{V}_{\mathcal{L}}$ of lattice \mathcal{L} . (ii) Isometric transformation W that decomposes as a product of disentanglers u and isometries w . (iii) Constraints fulfilled by disentanglers and isometries; see Eq. (40).

The examples of Figs. 10–16 used to illustrate this section corresponds to one-dimensional lattices for simplicity. Analogous constructions for two-dimensional lattices span three dimensions; see, e.g., in Refs. 32 and 33. Their graphical representation is significantly more involved and is not required in order to introduce the basic elements necessary for the present discussion. We postpone until Figs. 20 and 23 of Sec. V the explicit representation of three-dimensional structures.

B. Renormalization group flow

Successive applications of coarse-graining transformations $\{W, W', W'', \dots\}$ produce a sequence of increasingly coarse-grained lattices $\{\mathcal{L}, \mathcal{L}', \mathcal{L}'', \dots\}$ together with a sequence of effective, local Hamiltonians $\{H, H', H'', \dots\}$; see Fig. 13. If at each step the coarse-graining transformation projects onto the

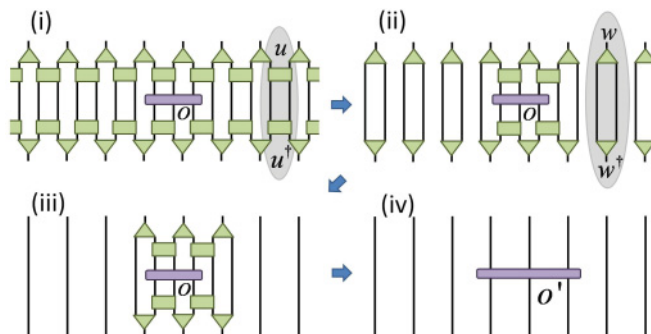


FIG. 11. (Color online) Coarse-graining of a local operator o acting on three contiguous sites of \mathcal{L} into a local operator o' acting on three contiguous sites of \mathcal{L}' . (i) Diagrammatic expression for $o' = W^\dagger o W$, where W decomposes as a product of disentanglers u and isometries w . (ii) Using that $u^\dagger u = I$, where I is the identity on two sites of \mathcal{L} , most disentanglers can be removed. (iii) Using that $w^\dagger w = I$, where I is the identity on one site of \mathcal{L}' , most isometries can be removed so (iv) o' acts as the identity in all but three sites of \mathcal{L}' .

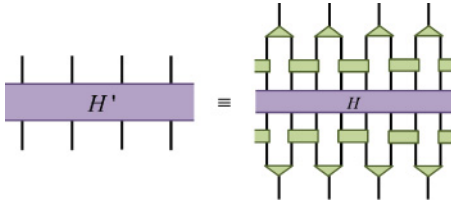


FIG. 12. (Color online) Effective Hamiltonian $H' \equiv W^\dagger H W$ expressed in terms of the original Hamiltonian H and disentanglers u and isometries w . If H is a sum of local terms, then H' can also be expressed as a sum of local terms; see Fig. 11.

low-energy subspace of the Hamiltonian, then the sequence of effective Hamiltonians defines a discrete renormalization group (RG) flow toward a fixed-point model that captures the low-energy/large-scale properties of the original model.

Suppose now that the original lattice \mathcal{L} is made of a finite number N of sites. Then the effective lattice \mathcal{L}' is made of a smaller number $N' = N/b$ of sites, where $b = 2$ in the example of Fig. 10(ii). In particular, after $O[\log_b(N)]$ applications of the coarse-graining transformation, lattice \mathcal{L} is reduced to a small lattice \mathcal{L}^{top} whose size is independent of N and such that H^{top} is amenable to exact diagonalization techniques. Note that a state $|\Psi^{\text{top}}\rangle \in \mathbb{V}_{\mathcal{L}^{\text{top}}}$ depends on a small number of parameters that is also independent of the original system size N .

C. Mera

A state $|\Psi^{\text{top}}\rangle \in \mathbb{V}_{\mathcal{L}^{\text{top}}}$ of this reduced lattice can be mapped into a state $|\Psi\rangle \in \mathbb{V}_{\mathcal{L}}$ of the original lattice by reversing the coarse-graining transformations; see Fig. 14,

$$|\Psi\rangle = W W' W'' \dots |\Psi^{\text{top}}\rangle. \quad (41)$$

This means that the top vector $|\Psi^{\text{top}}\rangle$ together with the sequence of transformations $\{W, W', W'', \dots\}$, as characterized by a sequence of disentanglers and isometries $\{\{u, w\}, \{u', w'\}, \{u'', w''\}, \dots\}$, can be used as an efficient representation a state $|\Psi\rangle \in \mathbb{V}_{\mathcal{L}}$. This representation is the MERA and can be used as a variational ansatz for, e.g., the ground state of H . This is achieved by optimizing the coefficients in $\{\{u, w\}, \{u', w'\}, \{u'', w''\}, \dots\}$ and $|\Psi^{\text{top}}\rangle$ so as to minimize the expectation value $\langle \Psi | H | \Psi \rangle$ using the techniques discussed in Ref. 33. More generally, by replacing $|\Psi^{\text{top}}\rangle$ with an isometry W^{top} that defines a χ^* -dimensional space \mathbb{C}_{χ^*} , a

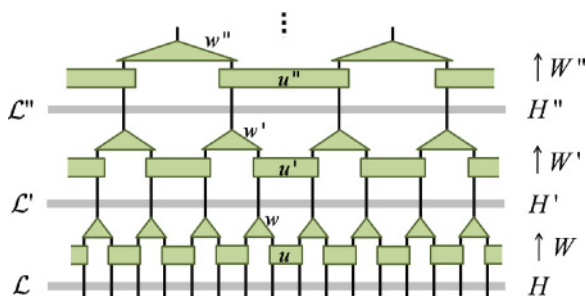


FIG. 13. (Color online) By composition, coarse-graining transformations $\{W, W', W'', \dots\}$ produce a sequence of increasingly coarse-grained lattices $\{\mathcal{L}, \mathcal{L}', \mathcal{L}'', \dots\}$ with effective Hamiltonians $\{H, H', H'', \dots\}$.

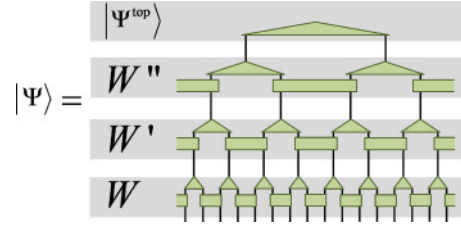


FIG. 14. (Color online) Example of a state of a lattice \mathcal{L} made of 16 sites, $|\Psi\rangle = W W' W'' |\Psi^{\text{top}}\rangle$, expressed as a MERA made of three layers of disentanglers and isometries corresponding to three coarse-graining transformations $W, W',$ and W'' .

whole subspace $\mathbb{V}^* \subseteq \mathbb{V}_{\mathcal{L}}$ can be represented. If $|\alpha\rangle$ denotes an orthonormal basis in \mathbb{C}_{χ^*} , then

$$|\Psi^\alpha\rangle = W W' W'' \dots W^{\text{top}} |\alpha\rangle, \quad \alpha = 1, \dots, \chi^* \quad (42)$$

is an orthonormal basis in $\mathbb{V}^* \subseteq \mathbb{V}_{\mathcal{L}}$. In this way, the MERA can be used to approximate, e.g., a low-energy subspace, including the ground state(s) and several low-energy excited states of H , as we will do in Sec. VI.

When the state $|\Psi\rangle$ in Eq. (41) is *translation invariant*, which is the case we have discussed so far, the MERA is specified with $O[\log_b(N)]$ parameters, namely those that characterize the $O[\log_b(N)]$ pairs of disentanglers and isometries $\{\{u, w\}, \{u', w'\}, \{u'', w''\}, \dots\}$. Thus, the MERA offers an efficient description of certain states of the lattice model, whose vector space $\mathbb{V}_{\mathcal{L}}$ has dimension $O[\exp(N)]$. [More generally, a generic MERA is specified by N -independent disentanglers and isometries and therefore depends on $O(N)$ parameters³³. In addition, a *scale-invariant* state $|\Psi\rangle \in \mathbb{V}_{\mathcal{L}}$ of the form (41) can be described using $O(1)$ parameters by choosing all disentanglers and isometries to be identical. The scale-invariant MERA is useful to represent the ground state of fixed points of the RG flow, whether corresponding to critical systems^{29,30,81,82} or to systems with topological order.^{83,84}

In Sec. VI we will use a translation invariant coarse-graining transformation for the deformed toric code model, which will lead to a translation invariant MERA for the ground state(s) and low-energy excited states of H_{TC}^x . However, for simplicity we will not attempt to use disentanglers in their full form (see Sec. VF for details) as a result of which the computational cost will grow as $O[\exp(\sqrt{N})]$. The limits of the small and

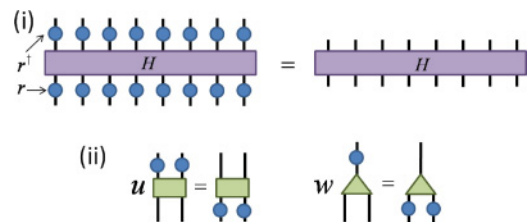


FIG. 15. (Color online) (i) Invariance of a Hamiltonian H under a global symmetry implemented by simultaneously acting with one-site transformation r on all sites of \mathcal{L} ; see Eq. (44). (ii) Disentangler u and isometry w invariant under the action of the single site transformation r , represented by a circle, acting on all upper/lower indices of these tensors. Note that the upper index of the isometry w is transformed according to r' , which might be a different representation of the symmetry group.

large magnetic fields of the Hamiltonian H_{TC}^x , i.e., $h_x = 0$ and $h_x = \infty$, correspond to fixed points of the RG flow, namely to a topologically ordered fixed point⁸³ and to a trivial fixed point, respectively. In these two cases, we will be able to represent the ground state with a scale-invariant MERA.

D. Global symmetry

Our goal is to coarse-grain a lattice model with a *local* symmetry. It is instructive to first consider the simpler and better understood case of a *global* symmetry.⁸⁵

Let r be a unitary transformation acting on one site of lattice \mathcal{L} , and let

$$R \equiv r^{\otimes N} \quad (43)$$

be the unitary transformation that results from applying the same transformation r on all sites of \mathcal{L} *simultaneously*. For instance, in the case where a site is described by a spin-1/2 degree of freedom, the one-site unitary transformation r could correspond to a Pauli matrix, say $r = i\sigma^x$, in which case $R = (i\sigma^x)^{\otimes N}$ corresponds to simultaneously rotating all spins in the lattice by an angle π in the \hat{x} direction.

The lattice Hamiltonian H is invariant under R if

$$RHR^\dagger = H, \quad (44)$$

an equation that can be represented diagrammatically as in Fig. 15(i). In this case, we say that the lattice model has a global symmetry R . Recall that if R is a global symmetry of H , then R^2 and R^{-1} are also a global symmetries of H and, more generally, the global symmetries of H always form a group. In the case of $r = i\sigma^x$, where $r^2 = I$, this group is Z_2 . We also notice in passing that this particular choice $r = i\sigma^x$ is actually a global symmetry of the deformed toric code Hamiltonian H_{TC}^x , since it is included as part of its local symmetry. There, R corresponds to the product of $N/2$ star operators A_s , chosen according to a checkerboard pattern.

The presence of a global symmetry is a fundamental property of a lattice model, since the eigenvectors of H are organized according to representations of the symmetry group. It is therefore of interest to consider a coarse-graining transformation W that preserves the global symmetry of a model. With exception of models with spontaneous symmetry breaking, which will not be considered here, the low-energy subspace automatically inherits the symmetries of a model and, in principle, there should be no need to enforce symmetry preservation during coarse-graining. However, due to the numerical (and therefore approximate) nature of W , the symmetry may be lost during coarse-graining, unless some measures are put in place to explicitly protect it.

In the case where W is the product of disentanglers u and isometries w , a global symmetry is automatically preserved if these tensors are chosen to be symmetric themselves, that is,

$$(r \otimes r)u(r \otimes r)^\dagger = u, \quad (r \otimes r)w(r')^\dagger = w, \quad (45)$$

where r' is a unitary matrix acting on a site of \mathcal{L}' , which in general will be transformed according to a different representation of the same symmetry group. The invariance of u and w implies that the action of the group commutes with these tensors; see Fig. 15(ii). As shown in Fig. 16, in this case

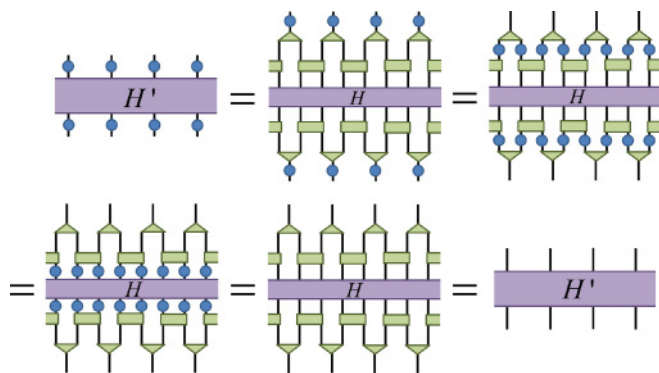


FIG. 16. (Color online) Sequence of equalities showing that a global symmetry $R = r^{\otimes N}$ of Hamiltonian H is exactly preserved by a coarse-graining transformation W that is the product of disentanglers u and isometries w , provided the latter are also invariant under transformation r ; Fig. 15. Indeed, the effective Hamiltonian $H' = W^\dagger H W$ is invariant under the global transformation $R' = (r')^{\otimes N}$.

indeed the coarse-grained Hamiltonian $H' = W^\dagger H W$ will also be invariant under the global transformation $R' \equiv (r')^{\otimes N}$.

Using symmetric tensors u and w not only ensures exact preservation of the global symmetry but also allows for important computational savings. On the one hand, symmetric tensors depend on fewer parameters than generic tensors, leading to a more compact variational ansatz. On the other hand, manipulating symmetric tensors (for instance, in order to compute the expectation value of a local observable) has lower computational cost than manipulating generic tensors.

E. Local symmetry

Let us now assume that the lattice model has a local symmetry. In this case the Hamiltonian H is invariant under unitary transformations that act on a small subset of neighboring sites, as exemplified by Eq. (21) for the deformed toric code Hamiltonian H_{TC}^x that is invariant under star operators A_s acting on four contiguous spins. This situation is diagrammatically represented in Fig. 17.

How can a local symmetry be exactly preserved during coarse-graining? And how can it be exploited to obtain a more compact variational ansatz and to reduce the computational cost of simulations, as in the case of a global symmetry? These questions were already addressed by Fradkin *et al.* in Ref. 86 and before it by the seminal work of Migdal *et al.* in Ref. 87. In the next section we take a fresh look at them, by applying the ideas of entanglement renormalization summarized in Sec. IV to this subject. The next section is indeed devoted to describe

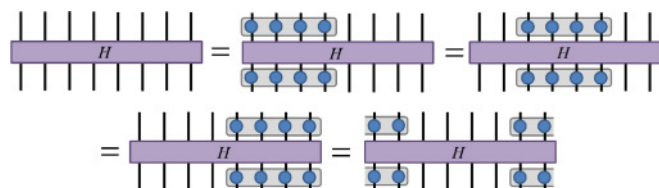


FIG. 17. (Color online) Diagrammatic representation of a Hamiltonian with a local symmetry. In this example the local symmetry is implemented by unitary transformations $r \otimes r \otimes r \otimes r$, acting on some blocks of four contiguous sites.

a coarse-graining transformation W for the deformed toric code Hamiltonian H_{TC}^x that explicitly preserves its local Z_2 symmetry.

V. COARSE-GRAINING OF A LATTICE MODEL WITH A LOCAL SYMMETRY

In this section we propose a coarse-graining transformation for lattice models with a local symmetry. For concreteness, we consider the toric code model⁴⁴ deformed with a magnetic field⁴⁹ as reviewed in Sec. II, which has a local Z_2 symmetry, although it is possible to generalize the present construction to quantum double models⁴⁴ with a generic discrete symmetry group using the results of Refs. 83, as well as to the more exotic context of string-net models⁸⁸ using the results of Ref. 84.

In order to motivate our construction, we start by discussing two other possibilities, namely (i) the use of a *bare* coarse-graining transformation that simply ignores the presence of the local symmetry altogether (as a result of which the local symmetry may not be preserved due to numerical errors) and (ii) the use of the (nonlocal) duality between the Z_2 lattice gauge theory and the quantum Ising model to apply a coarse-graining transformation to the Ising model instead. Then we present an overview of the strategy considered in this work, followed by a more detailed explanation of the two parts into which the coarse-graining transformation W splits: an exact transformation W_{exact} and a numerical transformation W_{num} . Finally, we also discuss how to compose several layers of coarse-graining and how to build a variational ansatz for low-energy states of the original model.

A. Motivation

Let us restate our goal. We would like to build an isometric transformation W ,

$$W^\dagger : \mathbb{V}_{\mathcal{L}} \rightarrow \mathbb{V}_{\mathcal{L}'}, \quad (46)$$

to coarse-grain the deformed toric code model,

$$H_{\text{TC}}^x \equiv -J_e \sum_s A_s - J_m \sum_p B_p - h_x \sum_j \sigma_j^x, \quad (47)$$

defined on a lattice \mathcal{L} made of $L \times L$ sites (or $2L^2$ spins), as reviewed in Sec. II, into an effective lattice \mathcal{L}' . For the case $J_e \gg J_m, h_x$, the entire low-energy subspace of H_{TC}^x is made of states that are invariant under the local symmetry [Eq. (3)]. We next discuss two simple options.

1. Bare coarse-graining

A first option is to proceed with a *bare* coarse-graining scheme that ignores the presence of the local Z_2 symmetry or, at most, merely exploits the global Z_2 symmetry given by

$$\left(\prod_j \sigma_j^x \right) H_{\text{TC}}^x \left(\prod_j \sigma_j^x \right) = H_{\text{TC}}^x. \quad (48)$$

In this case, one could consider a transformation W made of several types of disentanglers and isometries along the lines of the schemes used to study other two-dimensional lattice models with entanglement renormalization.^{31–33,35} Notice that the local symmetry, arguably a fundamental property of the

model, will in general not be protected against numerical errors that may occur during a bare coarse-graining transformation. In addition, several attempts in this direction (see, e.g., Fig. 2) indicate that, while it is possible to coarse-grain the system without exploiting the local symmetry, the computational cost of applying the bare approach to the deformed toric code is prohibitively large in the deconfined phase of the model, $h_x \leq h_x^{\text{crit}}$, due to the presence of large amounts of entanglement, as illustrated in Fig. 1.

2. Duality transformation

It might therefore be more convenient to exploit the local Z_2 symmetry. The symmetry introduces local constraints on the degrees of freedom of the model, implying that the vector space $\mathbb{V}_{\mathcal{L}}$ of the theory is redundantly large. It is possible to exploit these constraints to obtain an equivalent description in a smaller vector space and to then build the coarse-graining transformation directly on the reduced vector space. As reviewed in Sec. III A, when $J_e \gg J_m, h_x$, projection onto the low-energy subspace leads to the Z_2 lattice gauge theory, with Hamiltonian

$$H_{\text{LGT}} = - \sum_p B_p - h_x \sum_j \sigma_j^x, \quad (49)$$

where J_m was set to 1 without loss of generality. Recall that this model can be mapped into the quantum Ising model,^{42,69} as reviewed in Sec. III D,

$$H_{\text{Ising}} \equiv -h_x \sum_{\langle p, p' \rangle} \mu_p^x \mu_{p'}^x - \sum_p \mu_p^z, \quad (50)$$

where different topological sectors of H_{TC}^x correspond to different boundary conditions for H_{Ising} . This is the reduced description we were looking for.

Therefore a second option is to first transform the low-energy sector of the deformed toric code H_{TC}^x (with $J_e \gg J_m, h_x$) into the Ising model H_{Ising} and then to apply coarse-graining techniques to determine the ground-state phase diagram of the Ising model H_{Ising} , and, finally, to translate the results back to the deformed toric code model by undoing the duality transformation.

This is indeed a viable option. As a matter of fact, entanglement renormalization techniques have already been used to coarse-grain the quantum Ising model and study its ground-state phase diagram.^{31,32} In particular, with the specific layout of disentanglers and isometries proposed in Ref. 32, it was possible to study arbitrarily large lattices. The presence of a smaller amount of entanglement in the ground state of H_{Ising} , as compared to the ground state of H_{TC}^x , explains why the coarse-graining strategy has a lower computational cost for the Ising model than for the deformed toric code model.

This second approach can be extended to all those models with a local symmetry such that their low-energy subspace is dual to a simpler model. This is the case, for instance, of the quantum double model⁴⁴ for any discrete Abelian group Z_n , whose low-energy sector (if one allows only for certain type of excitations) corresponds to the Z_n lattice gauge theory, which in turn is dual to the n -state Potts model with a transverse magnetic field.⁸⁹ It seems, however, that for non-Abelian groups, an analogous duality transformation

produces a highly nonlocal model.⁹⁰ In spite of its simplicity, this second approach also has several drawbacks. Let us discuss two of them.

Vacancy. The duality transformation produces an Ising model with a vacancy that breaks translation invariance. While this may not be relevant in the thermodynamic limit, the presence of a vacancy in a finite system implies that the coarse-graining transformation cannot be homogeneous. As a result, for instance, the cost of simulations with the MERA increases from $O(\log L)$ for a translation invariant system to $O(L^2)$ for an inhomogeneous system.

Weak nonlocality. Another, more fundamental, limitation of using the duality is that this transformation is not local, as reflected by the presence of two nonlocal, boundary spins in the Ising model; see Fig. 9. We refer to the resulting model as being *weakly* nonlocal, since its Hamiltonian is still local in the bulk. A particular topological sector of H_{TC}^x can be studied by just fixing these boundary qubits to some product state, corresponding to fixing the boundary conditions of H_{Ising} , in which case the model is completely local. However, in a finite system it might be of interest to study processes that simultaneously involve several topological sectors of the model. These processes can still be studied with the resulting Ising model by allowing the boundary spins of Fig. 9 to be entangled with the rest of the spins. However, each boundary spin is coupled to $O(L)$ neighboring spins. This level of nonlocality is expected to produce large amounts of entanglement, with a subsequent increase in computational costs, possibly rendering the approach too expensive.

3. Beyond a global duality transformation

Finally, there are two fundamental reasons why in this work we explore an alternative coarse-graining transformation that is not based on simply mapping the low-energy subspace of H_{TC}^x into H_{Ising} .

One is that our ultimate goal is to develop a systematic approach that can also be applied to locally symmetric models and lattice gauge theories with a more general symmetry group, such as, e.g., non-Abelian groups, and not just to cases where a duality transformation exists to a simpler model (as is the case for finite Abelian groups Z_n ⁸⁹). In other words, we use the deformed toric code, arguably the simplest possible example, for illustrative purposes only. The coarse-graining transformation described below can be suitably generalized to quantum double models with arbitrary (possibly non-Abelian) discrete group (equivalently, to lattice gauge theories with an arbitrary discrete gauge group) by using the results of Ref. 83, as well as to string-net models⁸⁸ by using the results of Ref. 84.

The second reason is that we are interested in a scheme that can be generalized to models with a Hamiltonian where the local symmetry is explicitly broken (for the deformed toric code, by adding, e.g., an additional magnetic field $h_y \sum_j \sigma_j^y$ to H_{TC}^x) but such that the local symmetry is still recovered at low energies. In this broader context, the map to the Ising model is strongly nonlocal in that each σ_y is transformed into a string operator, whereas the coarse-graining scheme presented here can be suitably extended in a way that locality is strictly preserved, as discussed in subsequent work.

B. The strategy

Next we describe the coarse-graining transformation proposed in this work. The original lattice \mathcal{L} is transformed into an effective lattice \mathcal{L}' , where each plaquette of \mathcal{L}' is obtained by coarse-graining a block of four plaquettes of \mathcal{L} ; see Fig. 18. Thus, if the original lattice \mathcal{L} is made of $L \times L$ sites, the effective lattice \mathcal{L}' is made of $L' \times L'$ sites with $L' = L/2$. The coarse-graining is implemented by an isometric transformation W ,

$$W^\dagger : \mathbb{V}_{\mathcal{L}} \rightarrow \mathbb{V}_{\mathcal{L}'}, \quad (51)$$

that maps the original Hamiltonian H_{TC}^x into an effective Hamiltonian H' ,

$$H' \equiv W^\dagger H_{\text{TC}}^x W. \quad (52)$$

What makes transformation W special is that the effective H' *exactly* retains the local Z_2 symmetry of H_{TC}^x . This is accomplished by decomposing W into two parts,

$$W = W_{\text{exact}} W_{\text{num}}, \quad (53)$$

as illustrated in Figs. 18 and 19. The first part, W_{exact} , consists of a fixed sequence of CNOT gates (see Sec. III C) and single-spin projections. The second part is an isometric transformation W_{num} to be determined numerically.

In order to explain the role of W_{exact} and W_{num} , it is convenient to distinguish between two types of spins, depending on how the local Z_2 symmetry acts on them. We say that a spin is *constrained* by the local symmetry, or just “constrained,” if it is included in the support of at least one star operator A_s . In other words constrained spins are transformed nontrivially by the local symmetry. We say that a spin is “free” (that is, not constrained by the local symmetry) if no star operator A_s acts on it.

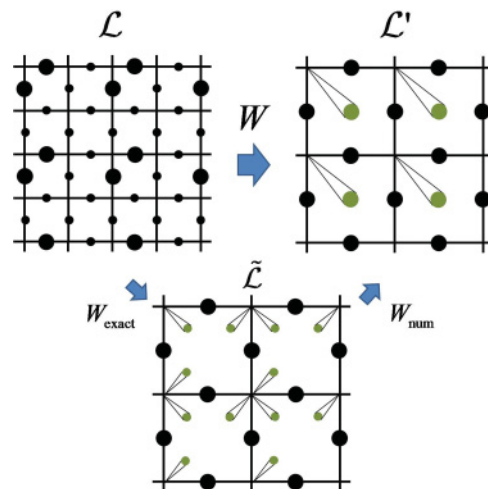


FIG. 18. (Color online) (Top) The coarse-graining transformation W transforms the lattice \mathcal{L} into the effective lattice \mathcal{L}' . Lattice \mathcal{L} has spins on its edges. Lattice \mathcal{L}' also has spins on its edges but, in addition, has an effective free spins sitting in the interior of each plaquette. (Bottom) Transformation $W = W_{\text{exact}} W_{\text{num}}$ breaks into an exact transformation W_{exact} , which produces an intermediate lattice $\tilde{\mathcal{L}}$ with constrained and free spins, and a numerical transformation W_{num} , which coarse-grains the free spins of lattice $\tilde{\mathcal{L}}$.

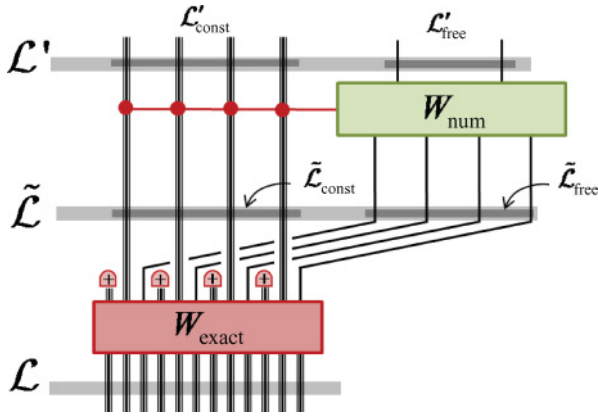


FIG. 19. (Color online) The proposed coarse-graining transformation W breaks into two pieces W_{exact} and W_{num} . W transforms the (constrained) spins of \mathcal{L} into the two types of spins present in the effective lattice \mathcal{L}' , namely constrained spins, represented by triple lines, and free spins, represented by single lines. W_{exact} acts on constrained spins, whereas W_{num} coarse-grains the free spins and acts on constrained spins diagonally on the σ^x basis.

Note that all the spins in \mathcal{L} are initially constrained, since each of them belongs to the support of two star operators A_s . In contrast, the coarse-grained lattice \mathcal{L}' will turn out to contain the above two types of degrees of freedom: *constrained* spins, sitting on the edges of \mathcal{L}' , and *free* spins, located inside the plaquettes of \mathcal{L}' ; see Figs. 18 and 19.

1. Analytic, exact coarse-graining

W_{exact} is applied only on constrained spins and its role is to transform some of these spins into free spins, while leaving other spins still constrained. It maps the original lattice \mathcal{L} into an intermediate lattice $\tilde{\mathcal{L}}$, Figs. 18 and 19,

$$(W_{\text{exact}})^\dagger : \mathbb{V}_{\mathcal{L}} \rightarrow \mathbb{V}_{\tilde{\mathcal{L}}}, \quad (54)$$

where the vector space $\mathbb{V}_{\tilde{\mathcal{L}}}$ contains both constrained and free spins,

$$\mathbb{V}_{\tilde{\mathcal{L}}} \cong \mathbb{V}_{\tilde{\mathcal{L}}}^{\text{const}} \otimes \mathbb{V}_{\tilde{\mathcal{L}}}^{\text{free}}. \quad (55)$$

The details of how W_{exact} manages to free some of the spins will be explained in Sec. V C. For now, we simply recall that the original lattice \mathcal{L} contains $2L^2$ constrained spins subject to L^2 star operators A_s , Eq. (3) [of which $L^2 - 1$ are linearly independent, Eq. (5)]. That is, there are only half as many star operators A_s as constrained spins. It is therefore plausible that, by properly reorganizing the vector space $\mathbb{V}_{\mathcal{L}}$, transformation W_{exact} can turn some of the constrained spins into free spins. W_{exact} is also in charge of eliminating some of the spins of lattice \mathcal{L} , namely those that after the sequence of CNOT gates are forced by the local symmetry to be in a fixed, unentangled state $|+\rangle$. An important feature of the transformation W_{exact} is that it is *exact*: not only it is specified analytically (as opposed to numerically), but it can also be exactly reversed, implying that no approximation errors are introduced while squeezing the low energy, locally symmetric sector of H_{TC}^x into the smaller vector space $\mathbb{V}_{\tilde{\mathcal{L}}}$ of lattice $\tilde{\mathcal{L}}$. Finally, W_{exact} depends only on a few structural aspects of the spin model, such as the fact that \mathcal{L} is a square lattice and how the local Z_2 symmetry acts on its

spins. In particular, W_{exact} is independent of the value of the magnetic field h_x in H_{TC}^x .

We note that W_{exact} is inspired in a similar transformation proposed in Ref. 83 for the (underformed) toric code, $h_x = 0$, and that was used to show that the model is a fixed point of the RG flow. Here we will use W_{exact} as part of a coarse-graining strategy valid for an arbitrary value of h_x .

2. Numerical, approximate coarse-graining

In contrast, transformation W_{num} is mostly concerned with free spins. Its goal is to coarse-grain these *free* spins into (*effective*) *free* spins, while acting only in a restricted way (to be explained below) on the constrained spins. It transforms the intermediate lattice $\tilde{\mathcal{L}}$ into the effective lattice \mathcal{L}' ; see Figs. 18 and 19,

$$(W_{\text{num}})^\dagger : \mathbb{V}_{\tilde{\mathcal{L}}} \rightarrow \mathbb{V}_{\mathcal{L}'}, \quad (56)$$

where the vector space $\mathbb{V}_{\mathcal{L}'}$ also contains both constrained spins and free spins,

$$\mathbb{V}_{\mathcal{L}'} \cong \mathbb{V}_{\mathcal{L}'}^{\text{const}} \otimes \mathbb{V}_{\mathcal{L}'}^{\text{free}}. \quad (57)$$

W_{num} is determined *numerically*, through some optimization procedure, and it is *approximate* in that the compression of the low-energy sector of H_{TC}^x into \mathcal{L}' may include errors whose size and implications have to be monitored. Finally, W_{num} depends on the specific details of Hamiltonian H_{TC}^x , namely on h_x .

3. Key properties

Before moving to a more detailed description of transformations W_{exact} and W_{num} in Secs. V C and V F, we reemphasize the two properties that the composite coarse-graining map W is designed to fulfill.

Preservation of locality. W transforms local operators in \mathcal{L} into local operators in \mathcal{L}' . In particular, we will see that the effective Hamiltonian H' remains local.

Preservation of the local Z_2 symmetry. The effective Hamiltonian H' retains the local Z_2 symmetry of the original Hamiltonian H_{TC}^x . The local symmetry is preserved *exactly* (in spite of the fact that W contains an approximate, numerical part W_{num}) and exploited to obtain a significant reduction in computational costs (when compared to a bare coarse-graining strategy).

It is the combination of these two properties, namely simultaneous preservation of locality and of the local Z_2 symmetry, that distinguishes the present approach from the two other options mentioned earlier in Sec. V A.

C. Exact transformation W_{exact}

Transformation W_{exact} consists of the sequence of CNOT gates and single-spin projections specified in Fig. 20, which maps blocks of four plaquettes of \mathcal{L} into single plaquettes of the intermediate lattice $\tilde{\mathcal{L}}$.

1. Free spins, unentangled spins, and constrained spins

The CNOT gates are applied according to a spatially periodic pattern that has a block of four plaquettes of \mathcal{L} as a unit cell (see the right side of Fig. 20). Their goal is to modify the support of

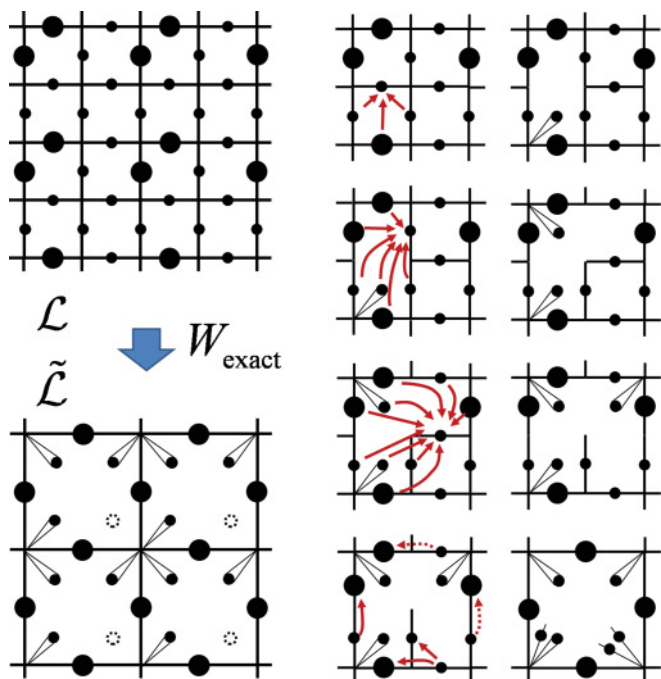


FIG. 20. (Color online) Exact coarse-graining transformation W_{exact} . All spins of the original lattice \mathcal{L} are equivalent. However, as a guide to the eye, larger circles are used to denote those spins that will remain constrained spins in $\tilde{\mathcal{L}}$. (Left) A region of the original lattice \mathcal{L} is mapped by W_{exact} into a region of the intermediate lattice $\tilde{\mathcal{L}}$. Blocks of four plaquettes of \mathcal{L} are mapped into single square plaquettes of $\tilde{\mathcal{L}}$, which contain three free spins and a vacancy in their interior. (Right) Detailed sequence of the CNOT gates, denoted by red arrows, applied to each block of four plaquettes in order to modify the support of the star operators A_s . For clarity, dashed arrows also show two CNOTs corresponding to neighboring unit cells. At the end of the sequence, there are three types of spins: free spins (green), unentangled spins (in state $|+\rangle$), and constrained spins. Unentangled spins are removed by single-spin projections and are therefore not present in $\tilde{\mathcal{L}}$.

star operators A_s . Some of these star operators, initially acting on four spins, end up acting as the operator σ^x on a single spin, while some other star operators end up acting on four spins of \mathcal{L} . This produces three types of spins as follows:

(i) Constrained spins that belong to the support of a star operator $A_{s'}$, where each star operator $A_{s'}$ acts on the four spins surrounding site $s' \in \tilde{\mathcal{L}}$. Constrained spins sit at the boundaries of the square plaquettes of $\tilde{\mathcal{L}}$.

(ii) Free spins, on which no star operator acts. They are depicted as green filled circles in Fig. 20. Free spins sit in the interior of a square plaquette of $\tilde{\mathcal{L}}$. Each free spin also belongs to a single-spin plaquette that emerges from one of the corners of a larger, square plaquette.

(iii) Unentangled spins, constrained to be an eigenstate of σ^x . They are produced by the last three CNOT gates on the right side of Fig. 20 and can be identified as those spins sitting on an open edge (each unentangled spin is depicted next to a ket $|+\rangle$). Note that any such spin must be in a product state. Indeed, if the collective state $|\xi\rangle$ of many spins is an eigenstate of σ_j^x (with positive eigenvalue $+1$) for some specific spin j , then that spin j cannot be entangled with the rest of the spins,

but must instead be in the state $|+\rangle$ [see Eq. (29)],

$$\sigma_j^x |\xi\rangle = |\xi\rangle \Rightarrow |\xi\rangle = |+\rangle_j \otimes |\xi_{\text{rest}}\rangle. \quad (58)$$

Note that this property is common to all the ground states of the Hamiltonians H_{TC}^x independently of the strength of the magnetic field h_x since the magnetic field commutes with the star operators. Transformation W_{exact} also includes projecting out any such spin, an operation that exactly preserve the state $|\xi_{\text{rest}}\rangle$ of the rest of the spins,

$$|\xi\rangle \xrightarrow{\text{projection}} \langle +_j | \xi \rangle = |\xi_{\text{rest}}\rangle. \quad (59)$$

Therefore these unentangled spins do not appear in the intermediate lattice $\tilde{\mathcal{L}}$.

In summary, constrained spins of the initial \mathcal{L} are either mapped into constrained spins of $\tilde{\mathcal{L}}$ (sitting at the boundary of a square plaquette) or free spins of $\tilde{\mathcal{L}}$ (sitting at the interior of square plaquette), or they are removed. This occurs in the following proportions:

$$\begin{array}{l} 8 \\ \text{constrained} \\ \text{spins} \in \mathcal{L} \end{array} \longrightarrow \begin{cases} 2 \text{ spins} \in \tilde{\mathcal{L}}_{\text{const}} \\ 3 \text{ spins} \in \tilde{\mathcal{L}}_{\text{free}} \\ 3 \text{ spins removed} \end{cases} \quad (60)$$

Lattice $\tilde{\mathcal{L}}$ can be thought of as being made of two square sublattices $\tilde{\mathcal{L}} = \tilde{\mathcal{L}}_{\text{const}} \cup \tilde{\mathcal{L}}_{\text{free}}$. The first contains constrained spins in its edges, and the second contains free spins (or vacancies) on its sites; see Fig. 21.

2. Transformed Hamiltonian

Under W_{exact} , the initial Hamiltonian H_{TC}^x is transformed into a new Hamiltonian

$$\tilde{H} \equiv (W_{\text{exact}})^\dagger H_{\text{TC}}^x W_{\text{exact}} \quad (61)$$

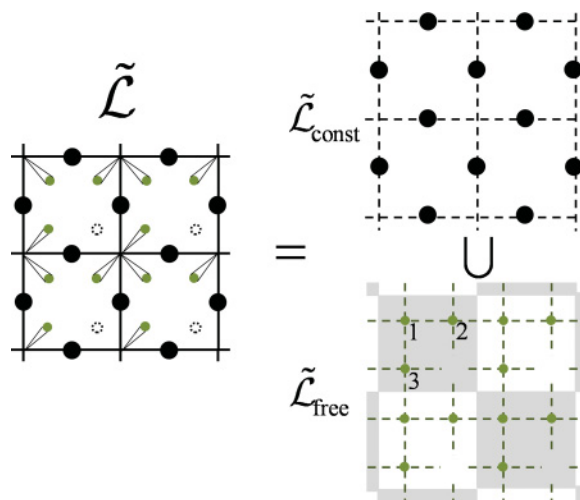


FIG. 21. (Color online) The intermediate lattice $\tilde{\mathcal{L}} = \tilde{\mathcal{L}}_{\text{const}} \cup \tilde{\mathcal{L}}_{\text{free}}$ decomposes as the union of a square sublattice $\tilde{\mathcal{L}}_{\text{const}}$ with a constrained spin on each of its edges and a square sublattice $\tilde{\mathcal{L}}_{\text{free}}$ with either a free spin or a vacancies on each of its sites. (Shading in $\tilde{\mathcal{L}}_{\text{free}}$ is used to indicate position relative to the plaquettes in $\tilde{\mathcal{L}}_{\text{const}}$).

that includes several types of terms,

$$\tilde{H} = -J_e \sum_{s' \in \tilde{\mathcal{L}}} A_{s'} - J_m \left(\sum_{p' \in \tilde{\mathcal{L}}} B_{p'} + \sum_{j \in \text{free}} \sigma_j^z \right) - h_x \tilde{K}_{\text{int}} \quad (62)$$

All these terms are represented in Fig. 22.

First, \tilde{H} has terms coming from the star operators A_s of H_{TC}^x . As just mentioned, some star operators A_s are simply eliminated (after being transformed into a single-spin operator σ^x), whereas others become four-spin star operators $A_{s'}$ acting on the sites of $\tilde{\mathcal{L}}$. Specifically, from every four star operators A_s acting on \mathcal{L} , only one becomes a star operator $A_{s'}$ acting on $\tilde{\mathcal{L}}$.

Hamiltonian \tilde{H} also has terms that originate in the plaquette operators B_p of H_{TC}^x . For every four plaquette operators acting on \mathcal{L} , three are transformed into single-site operators σ^z that act on the free spins of $\tilde{\mathcal{L}}$, whereas the fourth one becomes a seven-spin plaquette operator $B_{p'}$,

$$B_{p'} = \prod_{j \in p'} \sigma_j^z, \quad (63)$$

where the product includes the four spins at the boundary of plaquette $p' \in \tilde{\mathcal{L}}$ and the three free spins in its interior.

Finally, \tilde{H} also contains terms that result from transforming the magnetic field $-h_x \sum_j \sigma_j^x$ in H_{TC}^x . Under W_{exact} , the magnetic field becomes an interaction between free spins. There are two types of interactions: interactions within a square plaquette of $\tilde{\mathcal{L}}$, and interactions across the boundary between two plaquettes of $\tilde{\mathcal{L}}$, represented by yellow bulbs in Figs. 22(i) and 22(ii) respectively. Interactions within the plaquette are of the form $-h_x \sigma^x \otimes \sigma^x$ and couple pairs of first neighbor free spins. (Where the first neighbor of a free spin is a vacancy, the interaction is reduced to a magnetic field $-h_x \sigma^x$ acting on the free spin.) Interactions between free spins that belong to

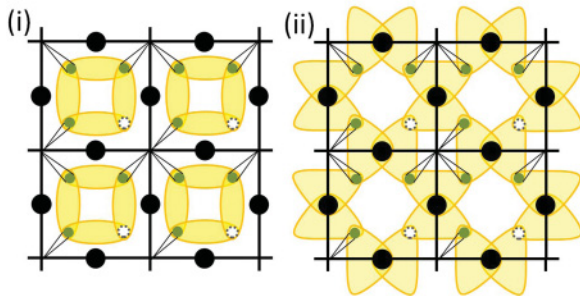


FIG. 22. (Color online) Depiction of the terms included in the transformed Hamiltonian \tilde{H} . From the structure of lattice $\tilde{\mathcal{L}}$, one can readily read the new star and plaquette operators of \tilde{H} [as explained in Fig. 5(ii)]. In addition, the magnetic field $-h_x \sum_i \sigma_i^x$ in H_{TC}^x gives rise to other interacting terms $-h_x \tilde{K}_{\text{int}}$, which are depicted as yellow shades. (i) Two-spin interaction $-h_x \sigma^x \otimes \sigma^x$ between nearest-neighbor free spins contained in the same plaquette. Note that in the presence of a vacancy, some of these terms become a magnetic field $-h_x \sigma^x$ acting on a free spin. (ii) Three-spin interaction $-h_x \sigma^x \otimes \sigma^x \otimes \sigma^x$ between two free spins on neighboring plaquettes and a constrained spin sitting at the boundary between those plaquettes. Again, the presence of a vacancy reduces the support of some of the interaction operators, which end up coupling one free spin and one constrained spin according to $-h_x \sigma^x \otimes \sigma^x$.

neighboring plaquettes of $\tilde{\mathcal{L}}$ are “mediated” by the constrained spin sitting at the boundary between the plaquettes, and it is of the form $-h_x \sigma^x \otimes \sigma^x \otimes \sigma^x$. (Again, where the interaction would involve a vacancy, it is reduced to the form $-h_x \sigma^x \otimes \sigma^x$ acting on a free spin and a constrained spin.)

The pattern of the interaction is suggestive. The free spins indeed are subject to interactions characteristic of a magnetically charged matter field. In this case the matter field transforms trivially under the action of the gauge group, since it belongs to \mathbb{V}_{LGT} on which by definition the constraints act as the identity operator (see Sec. III). It would then be tempting to interpret the free spins as an emergent matter field minimally coupled to the Hodge dual of the constrained spins that play the role of the magnetic photons. In this way the mechanism of confinement as dual superconductivity of the vacuum for the Z_2 lattice gauge theory becomes manifest.^{91,92}

D. Local implementation of the duality transformation

So far we have introduced transformation W_{exact} as a sequence of CNOT gates and single-spin projections and have described the Hamiltonian \tilde{H} resulting from transforming the deformed toric code Hamiltonian H_{TC}^x . Let us now take a minute to analyze these results.

W_{exact} has an interesting interpretation in relation to the duality transformation between the Z_2 lattice gauge theory and the quantum Ising model reviewed in Sec. III D. Indeed, looking back at Fig. 22 one can see that the three free spins inside a square plaquette of lattice $\tilde{\mathcal{L}}$ form a small, 2×2 quantum Ising model on their own (with a vacancy) in that they interact according to the Hamiltonian

$$-h_x \sum_{\langle j,k \rangle} \sigma_j^x \sigma_k^x - \sum_j \sigma_j^z \quad (64)$$

(where the interactions involving a free spin and the vacancy are reduced to a term $-h_x \sigma^x$ acting on the spin). Therefore, W_{exact} can be thought of as implementing a duality transformation inside each block of four plaquettes of \mathcal{L} . This visualization is useful. It tells us that the mechanism used by W_{exact} in order to remove degrees of freedom that are determined by the local symmetry (namely to transform some star operators A_s into operators σ^x acting on a single spin, which must consequently be in state $|+\rangle$, and to project out such spins) is the same that is used to transform the Z_2 lattice gauge theory into the Ising model. However, while the duality transformation is usually applied once globally on the whole system, W_{exact} applies an *independent* duality transformation on each block of four plaquettes of \mathcal{L} . This makes W_{exact} a fully local transformation, namely one that maps any local operator on \mathcal{L} into a local operator in $\tilde{\mathcal{L}}$.

The resulting tiny (three-spin) quantum Ising models inside the square plaquettes of $\tilde{\mathcal{L}}$, represented in Fig. 22(i), are not independent but rather patched together by further interactions represented in Fig. 22(ii). These interactions,

$$-h_x \sigma^x \otimes \sigma^x \otimes \sigma^x, \quad (65)$$

can be interpreted as Ising interactions between two free spins (one on each plaquette) that are *mediated* by the constrained spin sitting at the boundary between the two plaquettes. Specifically, depending on whether the constrained spin is

in state $|+\rangle$ or $|-\rangle$, the two free spins interact according to $-h_x \sigma^x \otimes \sigma^x$ or $h_x \sigma^x \otimes \sigma^x$. Again, this is reminiscent of the way the two nonlocal, boundary spins control the boundary conditions of the Ising model resulting from applying a global duality transformation; see Fig. 9.

E. Disentangling power of W_{exact}

Another relevant feature of W_{exact} is that it removes short-range entanglement present in the low-energy states of H_{TC}^x for $J_e \gg J_m, h_x$, and which has its origin in the presence of the local symmetry. To illustrate this point, we analyze the ground state of the transformed Hamiltonian \tilde{H} in the limits of small and large magnetic field h_x , where an analytic treatment is possible. Having established earlier that W_{exact} implements some sort of duality transformation to the quantum Ising model at a local level, it is easy to anticipate that, in these two limits, the free spins of $\tilde{\mathcal{L}}$ will be in an unentangled state, since this is the case in the analogous limits of the quantum Ising model.

1. Small magnetic field

For $h_x = 0$, the transformed Hamiltonian \tilde{H} of Eq. (62) becomes

$$-J_e \sum_{s' \in \tilde{\mathcal{L}}} A_{s'} - J_m \left(\sum_{p' \in \tilde{\mathcal{L}}} B_{p'} + \sum_{j \in \text{free}} \sigma_j^z \right). \quad (66)$$

Since in this case \tilde{H} is obtained by transforming the undeformed toric code Hamiltonian H_{TC} of Eq. (2), where all terms commute with each other, all terms in the above expression also commute with each other. Therefore for $h_x = 0$ the (four linearly independent) ground states of \tilde{H} are eigenstates of each individual Hamiltonian term. In particular, a term $-J_m \sigma^z$ acts on each free spin in $\tilde{\mathcal{L}}$, which therefore must be in state $|0\rangle$. Thus, for $h_x = 0$ any ground state of \tilde{H} factorizes as

$$|\xi_{\tilde{\mathcal{L}}}^{\text{const}}\rangle \otimes |\xi_{\tilde{\mathcal{L}}}^{\text{free}}\rangle, \quad (67)$$

where $|\xi_{\tilde{\mathcal{L}}}^{\text{const}}\rangle \in \mathbb{V}_{\tilde{\mathcal{L}}}^{\text{const}}$ is an entangled state of the constrained spins, whereas $|\xi_{\tilde{\mathcal{L}}}^{\text{free}}\rangle \in \mathbb{V}_{\tilde{\mathcal{L}}}^{\text{free}}$ is a product state of the free spins,

$$|\xi_{\tilde{\mathcal{L}}}^{\text{free}}\rangle = |0\rangle \otimes |0\rangle \otimes \cdots \otimes |0\rangle. \quad (68)$$

This factorization is not surprising; after all, the limit of small magnetic field h_x corresponds to the spin-polarized state of the quantum Ising model in the limit of a large transverse magnetic field (in the \hat{z} direction). And yet, it is a result that has important implications for the purposes of this article. It means that W_{exact} has transformed a robustly entangled state (the ground state of the undeformed toric code) into a state where a fraction of the spins are not entangled at all. This is the basis for a significant reduction in computational costs.

Following Ref. 83, we further notice that the state $|\xi_{\text{const}}\rangle$ for the constrained spins is again the ground state of the undeformed toric code. Indeed, after projecting out the free spins in state $|\xi_{\text{free}}\rangle$, the Hamiltonian in Eq. (66) becomes the toric code Hamiltonian of Eq. (2) defined now over the constrained spins of lattice $\tilde{\mathcal{L}}$. In other words, the models before and after the coarse-graining transformation are locally

identical, and the undeformed toric code is seen to be a fixed point of the RG flow.⁸³

For a finite $h_x \neq 0$ the free spins will no longer be in a product state but rather entangled between themselves and the constrained spins. However, for small values of h_x , the free spins are expected to still be only weakly entangled, an expectation confirmed by numerical simulations; see Fig. 1. Thus, one of the merits of transformation W_{exact} is that it reduces ground-state entanglement throughout the deconfined phase of the deformed toric mode model; see Sec. II.

2. Large magnetic field

We have just seen that transformation W_{exact} is capable of removing entanglement from the ground state of H_{TC}^x in the deconfined phase, a property that the present coarse-graining scheme will exploit to obtain a simplified description. It would be unfortunate, however, if W_{exact} would introduce additional entanglement in the other phase of H_{TC}^x , namely the spin-polarized phase; see Sec. II. This does not seem to be the case; see Fig. 1. In the limit of large magnetic field, this is easy to see.

Indeed, for very large h_x , and using that $J_e \gg J_m, h_x$, the deformed toric code Hamiltonian H_{TC}^x can be written as

$$-J_e \sum_s A_s - h_x \sum_j \sigma_j^x, \quad (69)$$

and its (unique) ground state is the spin-polarized state $|+\rangle \otimes |+\rangle \otimes \cdots \otimes |+\rangle$. It is clear from Eq. (31) that the sequence of CNOT gates leave this state invariant. Therefore, for large h_x , the ground state of \tilde{H} is also an unentangled, spin-polarized state.

F. Numerical transformation W_{num}

For a finite value of h_x , the ground state of \tilde{H} will be such that the free spins are entangled with the constrained spins of $\tilde{\mathcal{L}}$. The numerical transformation W_{num} coarse-grains the three free spins inside each square plaquette of the intermediate lattice $\tilde{\mathcal{L}}$ into an effective free spin of lattice \mathcal{L}' ; see Figs. 18 and 19.

Transformation W_{num} is required to fulfill two conditions. On the one hand, it must map local operators in $\tilde{\mathcal{L}}$ into local operators in \mathcal{L}' . This can be accomplished, for instance, by building W_{num} as a product of disentanglers and isometries, as explained in Sec. IV. On the other hand, W_{num} must commute with the local Z_2 symmetry. This is achieved by requiring that, at most, it acts on the constrained spins by means of operators that are diagonal in the σ^x basis. For instance, a unitary transformation

$$\exp(-i\varphi \sigma^x \otimes \sigma^x \otimes \sigma^y), \quad \varphi \in [0, 2\pi), \quad (70)$$

where the first and third Pauli matrices act on free spins and the middle one on a constrained spin, could be used to remove part of the entanglement introduced by the coupling of Eq. (65). Since this unitary transformation acts on the constrained spin diagonally on the σ_x basis, it commutes with any star operator $A_{s'}$ acting on that spin and therefore does not alter the action of the local Z_2 symmetry on $\tilde{\mathcal{L}}$.

In this work we use, for illustrative purposes, a simplified transformation W_{num} that is made only of isometries; see

Fig. 23. That is, we do not incorporate disentanglers in the numerical part of the coarse-graining transformation. This particular choice is clearly a limitation: local entanglement involving free spins is not removed by W_{num} and, as a result, it will accumulate over successive applications of the coarse-graining transformation W , in a way similar to what is observed using a tree tensor network (TTN) ansatz.⁷⁸ In Sec. VJ we will see that this choice of W_{num} limits the system sizes that can be addressed.

On the other hand, restricting our attention to a numerical transformation W_{num} that is made only of isometries also has several advantages from a pedagogical point of view. Its simplicity allows us to explicitly keep track of how the different terms in the initial Hamiltonian H_{TC}^x are transformed. In addition, the absence of numerical disentanglers in W_{num} (whose effect has already been studied in other two-dimensional systems^{31,32,35}) makes the role of W_{exact} in the whole coarse-graining, and in particular its disentangling power, more transparent. We refer to Ref. 93 for an example of a more complex W_{num} .

1. Effective free spins

Let us then see how our simplified choice of W_{num} (Fig. 23) transforms the system. Each isometry w in W_{num} simply maps the three free spins in the interior of a plaquette of $\tilde{\mathcal{L}}$ into an effective free spin,

$$w^\dagger : (\mathbb{C}_2)^{\otimes 3} \rightarrow \mathbb{C}_{\chi'}, \quad (71)$$

where \mathbb{C}_2 is the vector space of a free spin and $\mathbb{C}_{\chi'}$ is the χ' -dimensional space of an effective free spin.

The dimension χ' controls the degree of approximation introduced during coarse-graining. Ideally, it should be chosen large enough so $\mathbb{C}_{\chi'}$ can accommodate the support of the reduced density matrix of the three free spins (see, e.g.,

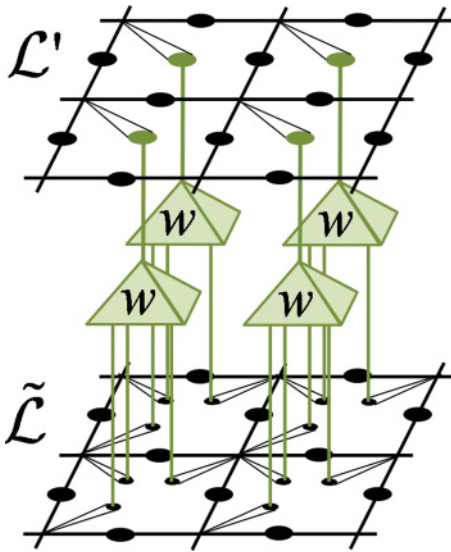


FIG. 23. (Color online) This simplified choice of the numerical transformation W_{num} consist of a tensor product of isometries w that coarse-grain the three free spins inside a square plaquette of $\tilde{\mathcal{L}}$ into an effective free spin of \mathcal{L}' ; see Eq. (71).

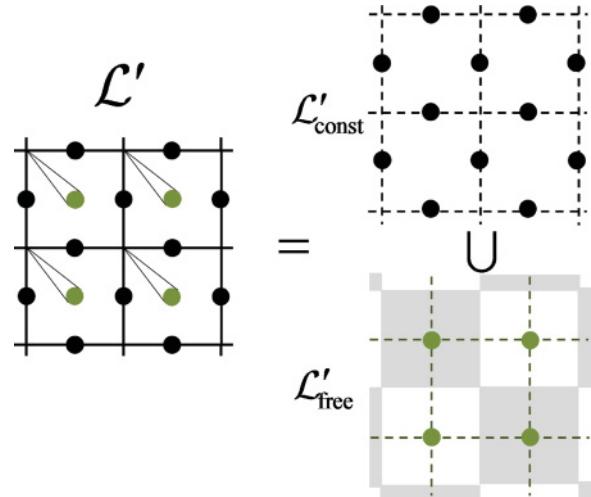


FIG. 24. (Color online) The effective lattice $\mathcal{L}' = \mathcal{L}'_{\text{const}} \cup \mathcal{L}'_{\text{free}}$ decomposes as the union of a square sublattice $\mathcal{L}'_{\text{const}}$ with a constrained spin on each of its edges and a square sublattice $\mathcal{L}'_{\text{free}}$ with an effective free spin on each of its sites. [Shading in $\mathcal{L}'_{\text{free}}$ is used to indicate position relative to the plaquettes in $\mathcal{L}'_{\text{const}}$.]

Ref. 78). Let χ'_ρ be the dimension of this support. The computational cost of the approach grows as a power of χ' . If, as a means to reduce the computational cost, χ' is chosen to be smaller than χ'_ρ , then the coarse-graining transformation becomes approximate.

For $h_x = 0$ and $h_x = \infty$ the free spins are in a product state and χ' can be chosen to be just 1, and the coarse-graining transformation becomes trivial. For other values of h_x , the free spins are entangled and a larger value of χ' must be used (Fig. 24).

2. Effective Hamiltonian

Under our simplified choice of W_{num} , Hamiltonian \tilde{H} is mapped into the effective Hamiltonian

$$H' \equiv (W_{\text{num}})^\dagger \tilde{H} W_{\text{num}} = W^\dagger H_{\text{TC}}^x W, \quad (72)$$

which again contains a number of terms (see Fig. 25)

$$H' = -J_e \sum_{s' \in \tilde{\mathcal{L}}} A_{s'} - J_m \left[\sum_{p' \in \tilde{\mathcal{L}}} B_{p'} + \sum_{j \in \text{free}} (\Sigma_j^z + \Sigma_j^x) \right] - h_x K'_{\text{int}}. \quad (73)$$

In this expression operators Σ^z for an effective free spin are obtained by coarse-graining the sum of the three σ^z 's acting on three free spins,

$$\Sigma^z \equiv w^\dagger (\sigma_1^z + \sigma_2^z + \sigma_3^z) w. \quad (74)$$

The operator Σ^x for an effective free spin is obtained by coarse-graining the sum of the interactions inside a block,

$$\Sigma^x \equiv w^\dagger (\sigma_1^x \sigma_2^x + \sigma_1^x \sigma_3^x + \sigma_2^x + \sigma_3^x) w. \quad (75)$$

In both Eqs. (74) and (75) the numbering of the σ^x and σ^z operators refers to the position of the free spin as reported in Fig. 21. The five-spin plaquette operator $B_{p'}$ is now the product of four σ^z 's corresponding to the constrained spins in plaquette $p' \in \mathcal{L}'$ and of Σ^z corresponding to the effective

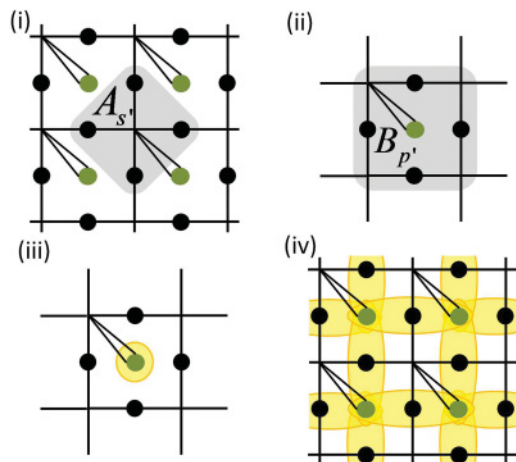


FIG. 25. (Color online) Terms that appear in the effective Hamiltonian H' , Eqs. (72) and (73). (i) Star operator $A_{s'}$ involving four constrained spins. (ii) Plaquette operator $B_{p'}$ involving four constrained spins and an effective free spin. (iii) Operators Σ^z [Eq. (74)] and Σ^x [Eq. (75)], acting on an effective free spin. (iv) Interactions between effective free spins on neighboring plaquettes of \mathcal{L}' , controlled by the a constrained spin.

free spin inside this plaquette. The term $-h_x K'_{\text{int}}$ collects interactions between effective free spins located in neighboring plaquettes, which are controlled by a constrained spin. What is significant about H' is that all operators are local (their support spans a small number of neighboring spins). We will see that this property is robust under successive coarse-graining transformations.

G. Exact preservation of the local symmetry

Let us discuss how the coarse-graining transformation W preserves the local Z_2 symmetry.

The local Z_2 symmetry acts on the original lattice \mathcal{L} by means of the star operators A_s , see Sec. II C. As we have seen above, W maps one-fourth of these operators into star operators $A_{s'}$ acting on the effective lattice \mathcal{L}' , whereas the remaining three-fourths of star operators A_s have been mapped into operators σ^x that act on spins that have been excluded from \mathcal{L}' . The roles played by W_{exact} and W_{num} in this process differ markedly. W_{exact} is in charge of transforming the star operators and removing three-fourths of them from the effective model. This is done analytically, so no numerical errors are introduced, and with a transformation that is independent of the magnetic field h_x , so the way in which the local Z_2 symmetry acts on \mathcal{L}' is always the same. In contrast, W_{num} coarse-grains the system numerically while avoiding to modify the way in which the local Z_2 symmetry acts. This is achieved by considering a transformation that commutes with all the star operators $A_{s'}$, and it implies that the local Z_2 symmetry will not be affected by the possible (numerical and truncation) errors that W_{num} may introduce.

H. Further coarse-graining

We can now apply a second coarse-graining transformation

$$(W')^\dagger : \mathbb{V}_{\mathcal{L}'} \rightarrow \mathbb{V}_{\mathcal{L}''}, \quad (76)$$

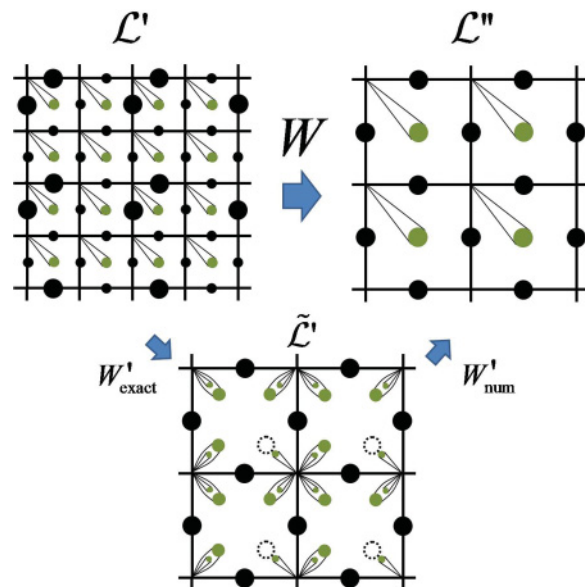


FIG. 26. (Color online) The coarse-graining transformation W' transforms a block of four plaquettes of the effective lattice \mathcal{L}' into a single plaquette of a new effective lattice \mathcal{L}'' . Note that lattice \mathcal{L}'' has the same local composition of constrained and free spins as \mathcal{L}' . Transformation W' again breaks into an exact transformation W'_{exact} , which produces an intermediate lattice $\tilde{\mathcal{L}}'$ and a numerical transformation W'_{num} .

which again breaks into an exact part W'_{exact} and a numerical part W'_{num} (see Figs. 26 and 27),

$$W' = W'_{\text{exact}} W'_{\text{num}}. \quad (77)$$

Transformation W' is very similar to transformation W , but it acts on a lattice made of both constrained and free spins, whereas W acts on a lattice made only of constrained spins. The exact transformation W'_{exact} acts on the constrained spins of \mathcal{L}' , and it does so by applying exactly the same sequence of CNOT gates and single-spin projections

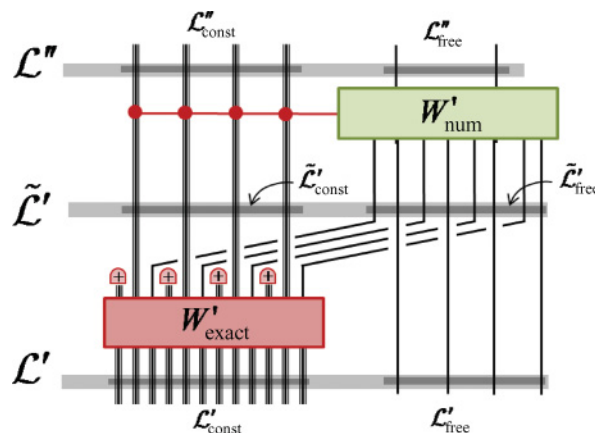


FIG. 27. (Color online) The coarse-graining transformation W' is composed of an exact transformation W'_{exact} that acts only on constrained spins and a numerical transformation W'_{num} that coarse-grains the fresh free spins obtained from W'_{exact} together with the free spins in \mathcal{L}' to produce the free spins of \mathcal{L}'' while acting on the constrained spins diagonally in the σ^x basis.

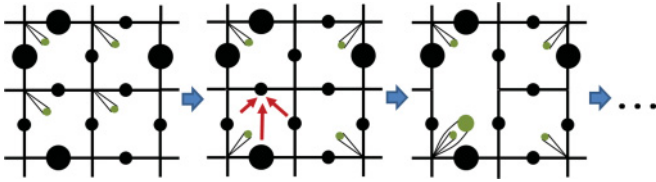


FIG. 28. (Color online) First round of the CNOT gates that constitute W_{exact} . Note that the free spins are simply ignored by the CNOT gates. (In the first step, we have repositioned the free spins for notational convenience.) The rest of the sequence of CNOT gates proceeds as in Fig. 20.

as W_{exact} while simply ignoring the free spins (see Fig. 28) to produce both constrained spins and fresh free spins. Then W'_{num} coarse-grains the free spins of \mathcal{L}' and the freshly produced free spins while acting on constrained spins diagonally in the σ^x basis.

The simplified numerical transformation W'_{num} considered in this work is made of isometries w' ,

$$(w')^\dagger : (\mathbb{C}_{\chi'})^{\otimes 4} \otimes (\mathbb{C}_2)^{\otimes 3} \rightarrow \mathbb{C}_{\chi''}, \quad (78)$$

that map the free spins in the interior of a plaquette of \mathcal{L}' (namely four effective free spins and three fresh free spins) into an effective free spin with vector dimension $\mathbb{C}_{\chi''}$, where again χ'' is the refinement parameter of the transformation.

W' maps local operators into local operators in very similar way as W does. In particular, the effective Hamiltonian H'' ,

$$H'' \equiv (W')^\dagger H' W', \quad (79)$$

can be seen to contain terms analogous to those of H' . (To illustrate this point, Fig. 29 shows the Hamiltonian terms that are obtained in transforming $-h_x K'_{\text{int}}$ in H' according to W'_{exact} , and which will produce $-h_x K''_{\text{int}}$.) With these observations, we can conclude that W' also preserves the locality of operators and the local Z_2 symmetry and that both properties will also be preserved under analogous subsequent coarse-graining transformations.

Note in Fig. 26 that lattices \mathcal{L}' and \mathcal{L}'' display an identical local pattern of constrained and free spins. Indeed, they both can be decomposed as the union of a sublattice for constrained spins and a square sublattice for free spins (see

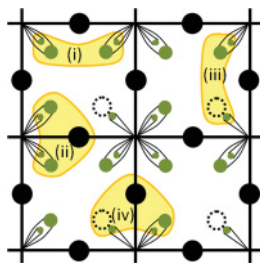


FIG. 29. (Color online) Examples of interactions contained in the term $(W'_{\text{exact}})^\dagger (-h_x K'_{\text{int}}) W'_{\text{exact}}$ of the Hamiltonian $(W'_{\text{exact}})^\dagger H' W'_{\text{exact}}$. (i) The interaction between two effective free spins is mediated by two fresh spins, on which it acts as $\sigma^x \otimes \sigma^x$. (ii) Analogous interaction across the boundary of a square plaquette, which involves a constrained spin. (iii)–(iv) In the presence of a vacancy, the interaction simply acts on one spin less.

Fig. 24). Therefore all following coarse-graining transformations W'', W''', \dots have the same structure of W' .

This allows us to consider a larger sequence of coarse-graining transformations $\{W, W', W'', \dots\}$. Each coarse-graining transformation halves the linear size of the lattice, reducing the number of constrained spins to one-fourth and, starting with W' , reducing the number of free spins also by one-fourth. Suppose that the initial lattice has $L \times L$ sites (or $2L^2$ constrained spins) with $L = 2^K$. After $(\log_2 L) - 1 = K - 1$ layers of coarse-graining, producing a sequence $\{\mathcal{L}, \mathcal{L}', \mathcal{L}'', \dots, \mathcal{L}^{\text{top}}\}$, the original lattice has been reduced to a small lattice \mathcal{L}^{top} , referred to as *top* lattice, with 2×2 sites or, equivalently, eight constrained spins and four free spins; see Fig. 30.

I. Top coarse-graining transformation W^{top} and topological degrees of freedom

The top lattice \mathcal{L}^{top} is mapped into a set of just three spins, collectively denoted \mathcal{L}^* , by a coarse-graining transformation W^{top} (see Figs. 30 and 31)

$$(W^{\text{top}})^\dagger : \mathbb{V}_{\mathcal{L}^{\text{top}}} \rightarrow \mathbb{V}_{\mathcal{L}^*}, \quad (80)$$

that decomposes as usual into exact and numerical parts, $W^{\text{top}} = W^{\text{top}}_{\text{exact}} W^{\text{top}}_{\text{num}}$.

Transformation W^{top} needs to be described explicitly, as it differs from previous transformations in a few aspects. Let us start with $W^{\text{top}}_{\text{exact}}$. The unit cell of four plaquettes on which the sequence of CNOT gates in Fig. 20 was defined amounts now to the whole lattice \mathcal{L}^{top} . As shown in Fig. 32, this implies that some CNOT gates are applied twice on the same control and target spins. Since a CNOT gate squares to the identity, such gates do not need to be applied. Another important difference is that in this case the sequence of CNOT gates does not produce any constrained spins. Indeed, the two spins that would otherwise be constrained (denoted as 1 and 2 in Fig. 32) are now free. This is due to the fact that toric

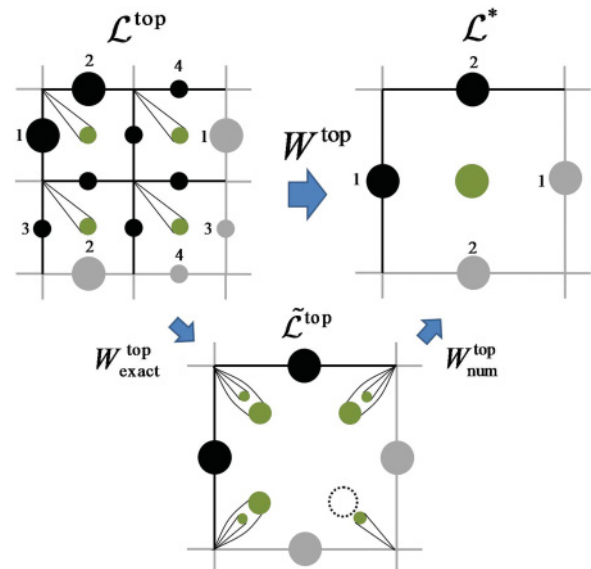


FIG. 30. (Color online) Graphical representation of \mathcal{L}^{top} , the intermediate lattice $\tilde{\mathcal{L}}^{\text{top}}$, and the final lattice \mathcal{L}^* made of just two topological spins and a free spin. Note the toric boundary conditions.

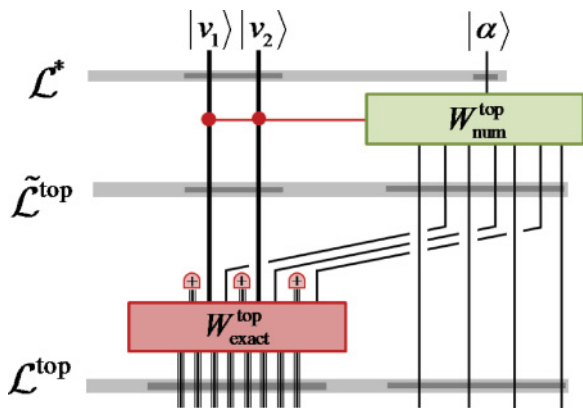


FIG. 31. (Color online) Transformation $W_{\text{exact}}^{\text{top}}$ produces two topological spins and three fresh new free spins. Transformation $W_{\text{num}}^{\text{top}}$ coarse-grains seven free spins into a single spin, while acting diagonally in a σ^x basis on the two topological spins. The topological sector (v_1, v_2) can be specified by setting the topological spins in the state $|v_1\rangle \otimes |v_2\rangle$. Index α labels an orthonormal basis $|\alpha\rangle \in \mathbb{C}_{\chi^*}$ of states of the final free spin. Each choice of topological sector (v_1, v_2) and of state $|\alpha\rangle$ labels one of 4χ orthonormal states $|\Psi_{(v_1, v_2)}^\alpha\rangle \in \mathbb{V}_{\mathcal{L}}$ of the original lattice \mathcal{L} , which can be reconstructed by undoing the sequence of coarse-graining transformations.

boundary conditions imply that a star operator A_s acting on these spins acts twice on each of them, and since the square of operator (σ^x) is the identity operator, the symmetry acts trivially. These two spins are very special. One can check that the string operators X_1 and X_2 of Eq. (6) acting on \mathcal{L}

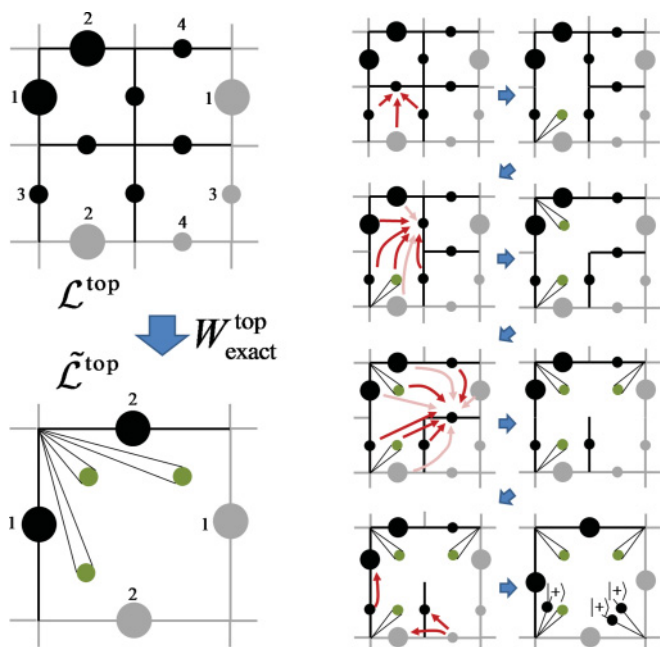


FIG. 32. (Color online) Lattices \mathcal{L}^{top} and $\tilde{\mathcal{L}}^{\text{top}}$, with toric boundary conditions, and sequence of CNOT gates and single-spin projections included in $W_{\text{exact}}^{\text{top}}$. For simplicity, the four free spins of \mathcal{L}^{top} have not been depicted. Note that due to the boundary conditions, in occasions two CNOT gates (denoted in lighter red) are applied twice on the same control and target spins, in which case they do not need to be applied, since the square of a CNOT gate is the identity operator.

are mapped, under coarse-graining, into operators σ_1^x and σ_2^x acting on these two spins. In other words, the state of these spins determines in which topological sector the model is. For this reason, instead of calling these spins free, we refer to them as *topological* spins. Incidentally, on a state $|\xi\rangle$ invariant under the local Z_2 symmetry, Eq. (3), operators X_1 and X_2 are equivalent to any operator obtained by multiplying them by star operators A_s . For instance, $A_s X_1$ is equivalent to X_1 ,

$$(A_s X_1)|\xi\rangle = X_1 A_s |\xi\rangle = X_1 |\xi\rangle, \quad (81)$$

where we have used that X_1 commutes with A_s and Eq. (3). Thus, by multiplication by star operators A_s allows us to locally deform the original support of X_1 and X_2 (namely the noncontractible cuts c_1 and c_2 in Fig. 3) without changing the action of these operators. In particular, operator $A_s X_1$ above (and any such products) will still be coarse grained by the present scheme into σ_1^x , and the same holds for deformations of the support of X_2 . On the other hand, the operators Z_1 and Z_2 of Eq. (8) acting on \mathcal{L} are mapped, under the present coarse-graining, into operators σ_1^z and σ_2^z acting on these two spins. (Note, however, that except in very special circumstances [e.g., when representing ground states of H_{TC}^x for $h_x = 0$, which also fulfill Eq. (4)] multiplying Z_1 and Z_2 by plaquette operators B_p will not produce an operator that will still be mapped into σ_1^z and σ_2^z . In other words, in our scheme, the support of X_1 and X_2 can be locally deformed without changing the properties of these operators, whereas this is not true of Z_1 and Z_2 , which must be supported on the specific noncontractible loops l_1 and l_2 shown in Fig. 3 in order to be mapped to σ^z operators on the topological spins.)

The role of transformation $W_{\text{num}}^{\text{top}}$ is to coarse-grain all free spins in $\tilde{\mathcal{L}}^{\text{top}}$ into a single free spin described by a vector space of dimension χ^* , while acting on the two topological spins diagonally in the σ^x basis. For each of four possible choices of the topological charges (v_1, v_2) , $W_{\text{num}}^{\text{top}}$ is characterized by an isometry w_{v_1, v_2} ,

$$(w_{v_1, v_2}^{\text{top}})^\dagger : (\mathbb{C}_{\chi^{\text{top}}})^{\otimes 4} \otimes (\mathbb{C}_2)^{\otimes 3} \rightarrow \mathbb{C}_{\chi^*}, \quad (82)$$

This completes our description of the coarse-graining transformations $\{W, W', W'', \dots, W^{\text{top}}\}$. By composition, they reduce the original lattice \mathcal{L} , made of $2L^2$ constrained spins with vector space $(\mathbb{C}_2)^{\otimes 2L^2}$, to just two topological spins and one free spin with vector space

$$\mathbb{V}_{\mathcal{L}^*} \cong \mathbb{C}_2 \otimes \mathbb{C}_2 \otimes \mathbb{C}_{\chi^*}. \quad (83)$$

J. Variational ansatz

Let $\{|\alpha\rangle\}$, $\alpha = 1, \dots, \chi$, denote an orthonormal basis of \mathbb{C}_{χ^*} . Then from states of \mathcal{L}^* of the form

$$|v_1\rangle \otimes |v_2\rangle \otimes |\alpha\rangle \in \mathbb{V}_{\mathcal{L}^*} \quad (84)$$

we can obtain a set of $4\chi^*$ orthonormal states $|\Phi_{v_1, v_2}^\alpha\rangle \in \mathbb{V}_{\mathcal{L}}$ of the original lattice \mathcal{L} by undoing the sequence of coarse-graining transformation,

$$|\Phi_{v_1, v_2}^\alpha\rangle \equiv W W' W'' \dots W^{\text{top}} |v_1\rangle \otimes |v_2\rangle \otimes |\alpha\rangle. \quad (85)$$

As is customary within MERA algorithms (see Sec. IV C), we use the set of isometric transformations $\{W, W', W'', \dots, W^{\text{top}}\}$ to define a variational ansatz for a

4χ -dimensional subspace \mathbb{V}^* of $\mathbb{V}_{\mathcal{L}}$. The variational parameters, denoted \vec{a} , are encoded in the isometric tensors (namely disentanglers and isometries) that form the numerical transformations $\{W_{\text{num}}, W'_{\text{num}}, W''_{\text{num}}, \dots, W_{\text{num}}^{\text{top}}\}$.

In order to obtain an approximation of the ground state(s) and lowest-energy excited state of Hamiltonian H_{TC}^x with this ansatz, the variational parameters \vec{a} are optimized to minimize the expectation value $E_{\vec{a}}$ of Hamiltonian H_{TC}^x on the subspace $\mathbb{V}^* \subset \mathbb{V}_{\mathcal{L}}$, namely

$$\min_{\vec{a}} E_{\vec{a}}, \quad E_{\vec{a}} \equiv \text{tr}(H_{\text{TC}}^x P_{\vec{a}}), \quad (86)$$

where $P_{\vec{a}}$ is a projector on subspace \mathbb{V}^* . This optimization can be performed using the optimization techniques extensively described in Refs. 33 and 78.

The ansatz used in this work is a hybrid between a MERA and a TTN. The exact transformation W_{exact} contains disentanglers (sequence of CNOT gates) and isometries (single-spin projections) and therefore it conforms to the definition of MERA. However, the simplified choice of numerical transformation W_{num} only has isometries, corresponding to a TTN. In the next section we refer to the ansatz as the *hybrid ansatz* to be able to distinguish it from the proper MERA used in Ref. 93 to recover the RG fixed points.

VI. BENCHMARK RESULTS

In this section we present the results of computations used to benchmark the performance of the present approach. We have used the hybrid ansatz introduced in the previous section to obtain an approximation to the ground state(s) and several excited states of the Hamiltonian H_{TC}^x for the deformed toric code model, for lattices \mathcal{L} of linear sizes $L = 4, 6, 8$, and 16.

The hybrid ansatz offers an explicit representation of the wave function of the system, from which it is possible to evaluate a number of quantities of interest. These include the expectation value of arbitrary local observables, such as the energy, but also of nonlocal observables, such as the disorder parameter $\langle X_3 \rangle$ and Wilson loops. In addition, it is possible to compute the overlap between different wave functions, leading to alternative tools to characterize the ground-state phase diagram of the model.

For the system sizes $L = 4, 6, 8$, it appears that the optimal choice of the numerical part of the coarse-graining is a simple TTN made of one layer with two isometries each mapping free spins into one free spin of dimension χ^{top} , followed by the top numerical isometry $W_{\text{num}}^{\text{top}}$. The refinement parameter χ^{top} , from now on denoted simply as χ , dominates the computational cost, which scales as $O(\chi^4)$, see Ref. 78. Energy minimization proceeds until no change is observed in the first 10 digits after 10 optimization steps. As an example of the required computational effort, obtaining the ground state and first excited state within the topological sector $(+, +)$ for $L = 4, 6$, and 8 took, on a desktop computer with two processors at 2 GHz, with 8 Gb of RAM, a total of 1, 5, and 8 h. Unless stated otherwise all the results we present here are obtained by fixing the value of χ to $\chi = 100$. In order to determine this value, we have performed a scaling analysis and found that this value is enough to produce a consistent approximation in both the topological and the spin-polarized

phase on the 8×8 torus. The scaling analysis is reported in the Appendix B.

Figure 2 illustrates one advantage the hybrid ansatz has over a TTN (resulting from a bare coarse-graining transformation, see Sec. V A). In the example, given the same computational cost, the hybrid ansatz leads to four more significant figures of accuracy for the ground-state energy in the deconfined phase of H_{TC}^x , which is robustly entangled; see also Fig. 1.

A. Local observables

1. Low-energy spectrum

Figure 33 shows the low-energy spectrum of H_{TC}^x as a function of the magnetic field h_x . It includes the energy of the ground state and first excited state of each of the four topological sectors (v_1, v_2) . As expected, for small h_x the ground-state energies in different topological sectors are very similar, whereas they depart from each other for values of the magnetic fields larger than $h_x \approx 0.3$, in which case the ground state in the sector $(+, +)$ becomes the global ground state.

The low-energy spectrum of H_{TC}^x can be obtained by minimizing the ansatz in either the whole vector space or within each specific topological sector (v_1, v_2) , which is achieved by fixing the topological spins to state $|v_1\rangle \otimes |v_2\rangle$. Since the second option needs to deal with fewer low-energy states at a time, it is generally more economical. In addition, in the spin-polarized phase, where ground states in different topological sectors have markedly different energies, restricting the minimization to a single topological sector, e.g., $(+, -)$, is important in order to get an accurate representation of its ground state. Indeed, for large h_x the ground state $|\Phi_{+,-}\rangle$

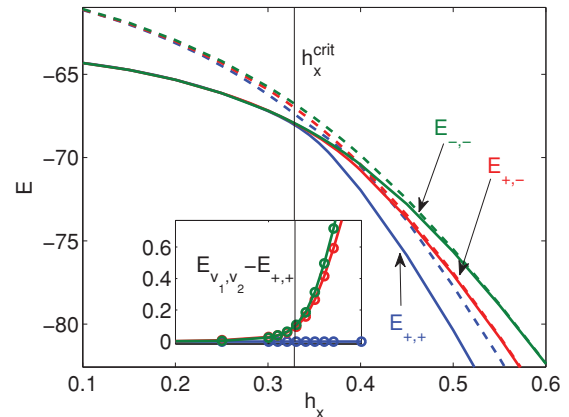


FIG. 33. (Color online) Lowest eigenvalues of H_{TC}^x as a function of the magnetic field h_x , for a system of linear size $L = 8$, corresponding to $8^2 \times 2 = 128$ spins. The two lowest energies in each topological sector (v_1, v_2) are plotted. The lowest energy in each sector is represented with a solid line while the second lowest with a dashed line. Different colors refer to different sectors. The energies in sector $(-, +)$ are identical to the energies in sector $(+, -)$. The inset shows the gap between the energy of the ground states in sector (v_1, v_2) and in the sector $(+, +)$. These gaps are very small for values of the magnetic field h_x smaller than some critical value $h_x^{\text{crit}} = 0.3285^{55}$ (denoted by a vertical line) and much larger for larger magnetic field h_x , see Fig. 34. These results were obtained with the hybrid ansatz with $\chi = 100$.

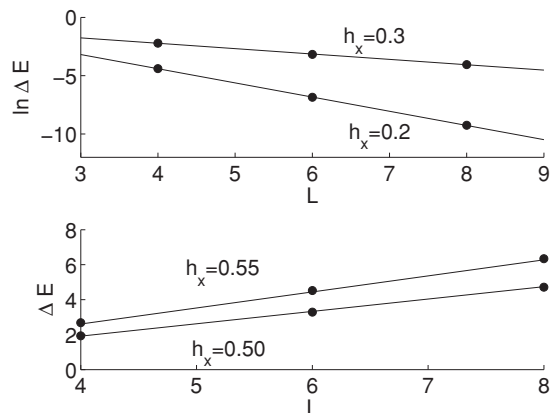


FIG. 34. (Top) Energy gap ΔE between the ground states of the topological sectors $(+, -)$ and $(+, +)$ [see Eq. (87)] as a function of the linear size L for $h_x = 0.2$ and 0.3 , corresponding to the deconfined phase of the deformed toric code model. In accordance with Eq. (12), ΔE decays exponentially with L . These results were obtained with the hybrid ansatz with $\chi = 100$. (Bottom) Energy gap ΔE between the ground states of the topological sectors $(+, -)$ and $(+, +)$ [see Eq. (87)] as a function of the linear size L for $h_x = 0.5$ and 0.55 , corresponding to the spin-polarized phase of the deformed toric code model. In accordance with Eq. (18), ΔE grows linearly with L . These results were obtained with the hybrid ansatz with $\chi = 100$.

is no longer a low-energy state of H_{TC}^x when the whole vector space is taken into account [as shown next, $|\Phi_{(+,+)}\rangle$ has $O(L)$ lower energy] and will not be properly captured through an unrestricted energy minimization.

2. Gaps between topological sectors

Figure 34 studies the gap

$$\Delta E \equiv E_{+,-} - E_{+,+} \quad (87)$$

between the ground states of the topological sectors $(+, -)$ and $(+, +)$ as a function of the system size. We obtain a clear confirmation of the exponential decay anticipated for the deconfined phase, see Eq. (12), as well as of the linear growth of the gap with system size in the spin-polarized phase, see Eq. (18).

3. Gap within the topological sector $(+, +)$

Recall that the ground state $|\Phi_{(+,+)}\rangle$ is the absolute ground state of H_{TC}^x for an arbitrary value of the magnetic field h_x . Figure 35 shows the energy gap $\Delta E_{+,+}$ within the topological sector $(+, +)$, as a function of h_x , and for $L = 4, 6, 8$. Note that the minimum of $\Delta E_{+,+}$ as a function of h_x closes roughly as $1/L$. This minimum occurs for a value of h_x that diminishes with L and a rough estimate of the critical value h_x^{crit} in the thermodynamic limit can be obtained by a large L extrapolation. However, a much more accurate estimate of h_x^{crit} is obtained by drawing the curves of $L\Delta E_{+,+}$ for increasing values of L in the range $L = 2, 4, 6, 8$. The position of intersections between those curves obtained at consecutive L (i.e., $L = 2$ with $L = 4$, $L = 4$ with $L = 6$ and $L = 6$ with $L = 8$) produces a sequence of $\tilde{h}_x^{\text{crit}}(L)$ that following the seminal work of Nightingale in Ref. 94 is expected to converge to the location of the fixed point as $\tilde{h}_x^{\text{crit}}(L) = h_x^{\text{crit}} - A/L^4$,

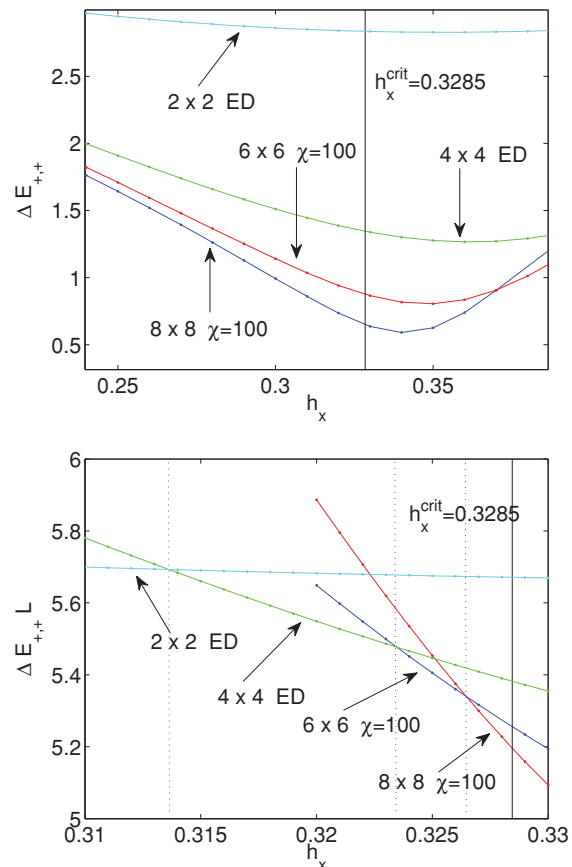


FIG. 35. (Color online) (Top) Gap $\Delta E_{+,+}$ between the ground state and first excited state of the topological sector $(+, +)$ as a function of the magnetic field h_x and for system sizes $L = 4, 6$, and 8 . (Bottom) Product of the systems size L times the energy gap $\Delta E_{+,+}$, plotted as a function of the magnetic field h_x . An estimate of $0.3267(5)$ for the critical magnetic field $h_x^{\text{crit}} = 0.3285(1)$ ⁵⁵ (denoted by a solid vertical line) is obtained by extrapolating, using the phenomenological renormalization group,⁹⁴ the sequence of intersections among curves obtained from systems with consecutive sizes (2–4, 4–6, and 6–8) identified by dotted vertical lines in the plot using the known L dependence for the sequence.⁵⁵

see Ref. 55. By fitting this expression to the sequence of intersections reported in the lower panel of Fig. 35 we obtain an estimate of the critical point $h_x^{\text{crit}} = 0.3267(5)$. This value is off the exact value 0.3285 ⁵⁵ by only 0.5%. The systematic error induced by limiting χ to $\chi = 100$ indeed pushes the transition toward smaller h_x since it limits the amount of entanglement in the ground state; however, its effects are surprisingly small.

B. Nonlocal observables

1. Disorder parameter

Figure 36 shows the disorder parameter $\langle X_3 \rangle$, introduced in see Sec. II B, which measures the formation of a condensate of magnetic vortices (or magnetic monopoles), as a function of the magnetic field h_x . Results for different system sizes $L = 2, 4, 6$, and 8 are presented. $\langle X_3 \rangle$ can clearly be used to distinguish the deconfined phase, where it vanishes, from the spin-polarized phase. Note that the drop of $\langle X_3 \rangle$ to zero for diminishing magnetic field h_x near the critical point becomes

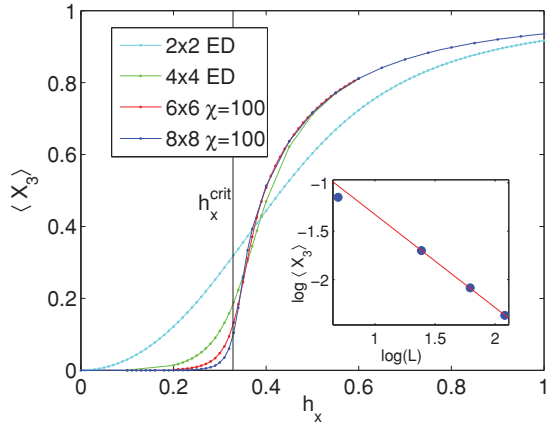


FIG. 36. (Color online) Disorder parameter $\langle X_3 \rangle$ as a function of the magnetic field h_x , for several lattice sizes. The critical magnetic field $h_x^{\text{crit}} = 0.3285(1)^{55}$ is denoted by a vertical line. The inset shows a log-log plot of $\langle X_3 \rangle$ at $h_x = h_x^{\text{crit}}$ as a function of L , from which we obtain an estimate of $0.96(5)$ for $2\beta/\nu$, whose current estimates are around 1.05 .⁷⁷

sharper with increasing system size L . For $L = 8$, we obtain an estimate $h_x^{\text{crit}} = 0.327 \pm 0.05$ for the critical magnetic field and $\beta = 0.33 \pm 0.02$ for the critical exponent β that should be compared with the best estimates coming from Monte Carlo simulations $\beta = 0.32652(15)$.⁷⁷ It is important to note that a direct measurement of this operator in Monte Carlo simulations is very challenging. Only recently, in the context of $U(1)$ LGT, an algorithm has been proposed to directly compute these kind of operators.⁹⁵

2. Wilson loops

Figure 37 shows the scaling of Wilson loops, see Sec. II B, for the ground state of the topological sector $(+, +)$. In this

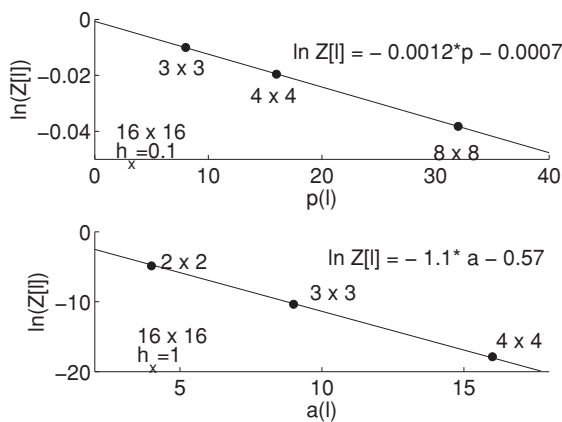


FIG. 37. (Top) Wilson loop $\langle Z[l] \rangle$ as a function of the perimeter $p(l)$ of loop l , on a 16×16 lattice with magnetic field $h_x = 0.1$, corresponding to the deconfined phase. Note the exponential decay of $\langle Z[l] \rangle$ as a function of the perimeter $p(l)$ of loop l , or *perimeter law*; see Eq. (17). (Bottom) Wilson loop $\langle Z[l] \rangle$ as a function of the area $a(l)$ of loop l , on a 16×16 lattice with magnetic field $h_x = 1$, corresponding to the spin-polarized phase. Note the exponential decay of $\langle Z[l] \rangle$ as a function of the area $a(l)$ of loop l , or *area law*; see Eq. (20).

case, a lattice of 16×16 sites, or $16^2 \times 2 = 512$, spins was considered for a magnetic field $h_x = 0.2$ (deconfined phase) and $h_x = 1$ (spin-polarized phase). For these values of the magnetic field the system is away from the critical point, as reflected in a drop in the amount of ground state entanglement; see Fig. 1. This allows the hybrid ansatz to reliably represent much larger lattices with just $\chi = 100$.

For $h_x = 0.2$ our results confirm that a Wilson loop decays exponentially fast with the size of the loop according to a perimeter law, as it is characteristic of the deconfined phase. Instead, for $h_x = 1$ the decay is exponential in the area encircled by the loop, as it is characteristic of the spin-polarized phase.

C. Wave function fidelities

1. Ground-state fidelities

The overlap or fidelity $\langle \Phi(h_x) | \Phi(h'_x) \rangle$ between the ground state of H_{TC}^x for two values h_x, h'_x of the magnetic field can be used as an alternative way to detect the presence of phases in the model and the location of their boundaries. Indeed, the ground-state wave function is somewhat similar within a phase and experiences a radical change when the system undergoes a phase transition, with these two facts being captured by the ground-state fidelity. Interestingly the characterization of phase boundaries using the fidelity does not require the knowledge of the order parameters. Here we will focus on the intensive fidelity $f(h_x, h'_x)$,^{96–104} defined through

$$\log f(h_x, h'_x) \equiv \frac{1}{L^2} \log(|\langle \Phi(h_x) | \Phi(h'_x) \rangle|). \quad (88)$$

The present approach yields an explicit representation of the ground-state wave function, from which computing overlaps is straightforward (this is true of the hybrid ansatz used in this work but not in the more general case where W_{num} also contains disentanglers⁹³). Figure 38 shows the logarithm of the intensive fidelity

$$f_0(h_x) \equiv f(h_x, 0) \quad (89)$$

between the ground states of H_{TC}^x in the topological sector $(+, +)$ for $h_x = 0$ and another value $h_x \geq 0$; as well as the

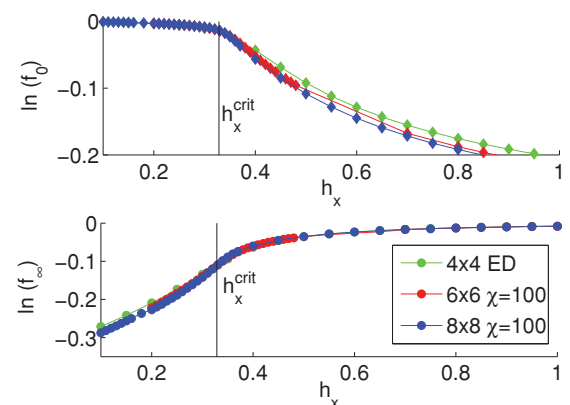


FIG. 38. (Color online) Logarithm of the intensive fidelities $f_0(h_x)$ and $f_\infty(h_x)$ as a function of the magnetic field h_x for different values $L = 4, 6$, and 8 of the system size. The critical magnetic field $h_x^{\text{crit}} = 0.3285(1)^{55}$ is denoted by a vertical line.

logarithm of the intensive fidelity

$$f_\infty(h_x) \equiv f(h_x, \infty) \quad (90)$$

between the ground states of H_{TC}^X in the topological sector $(+, +)$ for $h_x = \infty$ and another value $h_x \geq 0$. Fidelity $f_0(h_x)$ shows a markedly different behavior for small magnetic fields roughly smaller than h_x^{crit} [corresponding to the deconfined phase, to which $|\Phi(0)\rangle$ also belongs to] and for large magnetic fields, where the fidelity vanishes. An analogous behavior is also observed for $f_\infty(h_x)$.

2. Topological fidelities

For $h_x = 0$, the ground states in two topological sectors only differ in the expectation value of operators X_1 and X_2 ; see Sec. II A. One can map, e.g., the ground state $|\Phi_{+,+}\rangle$ of topological sector $(+, +)$ into the ground state $|\Phi_{+,-}\rangle$ of topological sector $(+, -)$ by just applying operator Z_2 of Eq. (8), namely $|\Phi_{+,-}\rangle = Z_2|\Phi_{+,+}\rangle$. Therefore $\langle\Phi_{+,+}|Z_2|\Phi_{+,-}\rangle = 1$ and the *topological* fidelity $f_{+,+}^{+,-}$ between these two sectors, defined as

$$\log(f_{+,+}^{+,-}) \equiv \frac{1}{L^2} \log(\langle\Phi_{+,+}|Z_2|\Phi_{+,-}\rangle), \quad (91)$$

is maximal, $f_{+,+}^{+,-} = 1$, for $h_x = 0$. More generally, the *topological* fidelity between sectors (v_1, v_2) and (v'_1, v'_2) , defined as

$$\log(f_{v_1, v_2}^{v'_1, v'_2}) \equiv \frac{1}{L^2} \log \langle\Phi_{v_1, v_2}|(Z_1)^{w_1}(Z_2)^{w_2}|\Phi_{v'_1, v'_2}\rangle, \quad (92)$$

where w_i is 0 if $v_i = v'_i$ and 1 otherwise, also fulfills

$$f_{v_1, v_2}^{v'_1, v'_2} = 1(h_x = 0). \quad (93)$$

For $h_x \neq 0$ Eq. (93) is no longer expected to hold. In particular, in the limit of large magnetic field h_x a simple analytical characterization of the ground states $|\Phi_{v_1, v_2}\rangle$ exists and can be used to show, e.g., that $|\langle\Phi_{+,+}|Z_2|\Phi_{+,-}\rangle| = L^{-1/2}$, so $f_{+,+}^{+,-}$ vanishes for large L . More generally,

$$f_{v_1, v_2}^{v'_1, v'_2} = 0(h_x = \infty, L = \infty). \quad (94)$$

For intermediate values of h_x , the topological fidelity is expected to remain close to 1 in the deconfined phase and sharply decay in the spin-polarized phase. Figure 39 for $\log(f_{+,+}^{+,-})$ as a function of h_x shows that this is indeed the case. In addition, the data for different values of L collapse into a single curve in the deconfined phase if $\log(f_{+,+}^{+,-})$ is multiplied by L , whereas in the spin-polarized phase the data collapse into a single curve when $\log(f_{+,+}^{+,-})$ is directly plotted. This is reminiscent of the two possible behaviors of Wilson loops, namely perimeter versus area law; see Fig. 37. After all, operators Z_1 and Z_2 can be understood as Wilson loops with noncontractible support.

VII. DISCUSSION

In this article we have proposed a coarse-graining transformation for lattice models with a local symmetry that simultaneously preserves locality and the symmetry, while exploiting the latter to significantly reduce computational costs. This coarse-graining transformation, made of an analytical part W_{exact} and a numerical part W_{num} , gives rise to a variational

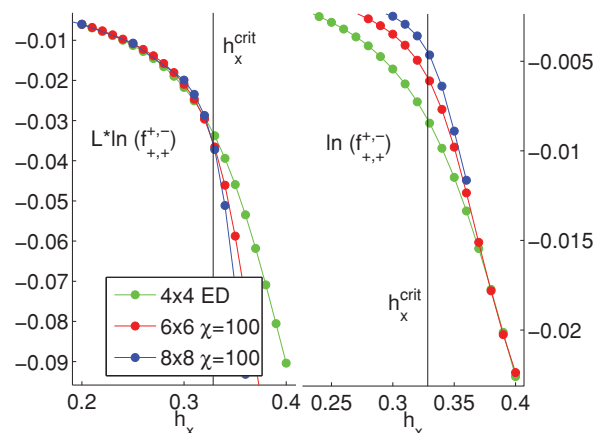


FIG. 39. (Color online) Logarithm of the intensive *topological* fidelity $f_{+,+}^{+,-}$ as a function of the magnetic field h_x . In the deconfined phase, $f_{+,+}^{+,-}$ remains large (its logarithm remains close to zero), indicating that the ground states $|\Phi_{+,+}\rangle$ and $|\Phi_{+,-}\rangle$ differ mostly on their topological spins but are otherwise very similar. This trend changes for larger magnetic fields h_x . As we enter the spin-polarized phase, the ground states $|\Phi_{+,+}\rangle$ and $|\Phi_{+,-}\rangle$ differ structurally, and modifying the topological spins of, e.g., $|\Phi_{+,-}\rangle$ no longer produces a good approximation to $|\Phi_{+,+}\rangle$. (Left) Data collapse occurs in the deconfined phase when we plot $L \log(f_{+,+}^{+,-})$. The critical magnetic field $h_x^{\text{crit}} = 0.3285(1)$ ⁵⁵ is denoted by a vertical line. (Right) Instead, plotting $\log(f_{+,+}^{+,-})$ leads to data collapse in the spin-polarized phase. This behavior is expected as explained in the main text below Eq. (94).

ansatz for the ground state(s) and low-energy states of the lattice model. Here we have focused on a simplified form of the ansatz, a hybrid between a TTN and the MERA, in which W_{num} does not contain disentanglers (although W_{exact} does). The computational cost of the resulting approach grows exponentially with the linear size L of the lattice, severely restricting the size of systems that can be analyzed, although it permits us to consider systems well beyond the scope of exact diagonalization techniques.

By adding disentanglers to W_{num} , it is possible to remove more entanglement from the ground state. The resulting ansatz is a proper MERA, with which much larger systems can be addressed. In addition, as explained in Ref. 93, under coarse-graining transformations the ground state of H_{TC}^X for a small magnetic field h_x can now be seen to flow back to the $h_x = 0$ fixed point of RG flow, which has a richer, local $Z_2 \times Z_2$ symmetry, whereas the ground state for $h_x > h_x^{\text{crit}}$ flows to the spin-polarized RG fixed point characterized by an infinite h_x .

A. Generalizations

The coarse-graining transformation proposed in this article can be generalized to more complex settings in a number of ways.

1. Static electric charges

Throughout the article we have assumed that the state of the lattice model satisfies the star constraints of Eq. (3), corresponding to the absence of electric charges. However, the coarse-graining scheme and related ansatz can be readily adapted to the case where one or several star constraints are

violated on specific sites, provided that the state ξ of the lattice is constrained to satisfy

$$A_s|\xi\rangle = -|\xi\rangle \quad (95)$$

on those specific sites. Indeed, the only change that is required in the coarse-graining scheme is that when the star operator is eventually transformed by a sequence of CNOT gates into a single-spin operator $-\sigma^x$, the spin on which it acts, forced now to be in state $|-\rangle$ instead of $|+\rangle$, is projected out accordingly.

In this way one could study the ground state of the system in the presence of two electric charges separated a distance l and obtain the ground-state energy as a function of l , from which the string tension can be evaluated.

2. Magnetic field in the xz plane

If the toric code Hamiltonian is perturbed by adding a magnetic field $-\sum_j (h_x \sigma_j^x + h_z \sigma_j^z)$ on the xz plane, a lattice model with local Z_2 symmetry can still be recovered by adding dummy spin variables, corresponding to matter field, on the sites of lattice \mathcal{L} ; see Ref. 105. In that case the local Z_2 symmetry can still be exploited, but in a trivial sense (the dummy spin variables are factored back out as part of the coarse-graining transformation) that appears to have no advantage to the case of an arbitrary perturbation, which is considered next.

3. Arbitrary perturbation of the toric code

In this work we have focused on a perturbation of the toric code Hamiltonian H_{TC} in Eq. (2) that breaks its $Z_2 \times Z_2$ local symmetry for $h_x = 0$, generated by both star operators A_s and plaquette operators B_p , into a local Z_2 symmetry for $h_x \neq 0$ generated by star operators only. A generic perturbation of Hamiltonian H_{TC} will break the local symmetry completely. However, as recently proven by Bravyi, Hastings, and Michalakakis in Ref. 106, topological phases are robust under arbitrary (sufficiently weak) perturbations of the Hamiltonian.

For a perturbation that completely breaks the local $Z_2 \times Z_2$ symmetry of the toric code model, say a weak magnetic field in a direction $\hat{r} = (r_x, r_y, r_z)$ differing from directions $\pm\hat{x}$ and $\pm\hat{z}$ ^{107,108}, we can modify W_{exact} so it no longer projects spins into $|+\rangle$ state. The sequence of CNOT gates in Fig. 20, which produces six spins per plaquette on which either operator $-J_e \sigma^x$ or operator $-J_e \sigma^z$ is acting, is now followed by an extended numerical transformation W_{num} that acts on all these six spins to produce an effective spin inside each plaquette of \mathcal{L}' . For small values of the perturbation, the sequence of CNOT gates will still map a robustly entangled ground state into a weakly entangled ground state, lowering significantly the computational cost of the approach, while the use of disentanglers as part of W_{num} is expected to again produce a flow back to the RG fixed point given by the undeformed toric code Hamiltonian H_{TC}^x .

4. Quantum double models and string-net models

The analytic transformation W_{exact} used in this work is, in essence, equivalent to the RG transformation proposed in Ref. 83 to show that the toric code model is a fixed point of the RG flow. In that work, analogous analytical transformations

were proposed also for generalizations of the toric code, which corresponds to the quantum double of the Z_2 group, to models based on the quantum double of any discrete group G .⁴⁴ In the appropriate regime, the low-energy sector of the quantum double model with group G corresponds to a lattice gauge theory with the same gauge group. A similar analysis was subsequently carried forward in Ref. 84 for string-net models.⁸⁸

The analytical transformations described in Refs. 83 and 84 for the fixed-point Hamiltonians of quantum double and string-net models map robustly entangled spins *locally* into spins that are in a product state and can therefore be factored out (or projected out) from the coarse-grained system. They can again be used as the basis for a generalized analytical transformation W_{exact} , which needs to be supplemented with a numerical transformation W_{num} when the fixed-point Hamiltonian is deformed with an arbitrary perturbation. In this way, we obtain a coarse-graining scheme for deformed quantum double models (equivalent in the appropriate regime to lattice gauge theories) and string-net models, as well as corresponding tensor network ansätze for their ground-state wave functions.

5. Renormalization of PEPS

The use of an analytical transformation W_{exact} as part of a coarse-graining procedure can be also exported to the domain of approaches based on PEPS (also referred to as TPS). This can occur in two different contexts.

On the one hand, given a PEPS representation for a state $|\xi\rangle$ (e.g., the ground state of Hamiltonian H_{TC}^x) with a local Z_2 symmetry, an important task is to evaluate the tensor network corresponding to the scalar product $\langle \xi | \xi \rangle$ (and related quantities), which plays a central role in the computation of expectation values of observables and various optimization algorithms. The tensor network for $\langle \xi | \xi \rangle$ can be evaluated by a number of different methods, such as corner transfer matrix (CTM) methods,^{109,110} MPS techniques,^{14,15} or the tensor entanglement renormalization group^{17,20,21} (TERG). All these methods proceed by coarse-graining the tensor network for the scalar product $\langle \xi | \xi \rangle$ (as opposed to coarse-graining a tensor network for the state $|\xi\rangle$), with a cost that depends on the amount of entanglement in the system. This cost can again be significantly reduced if the coarse-graining incorporates analytic local preprocessing along the lines of the transformation W_{exact} discussed in this work.

On the other hand, a PEPS representation for the same state $|\xi\rangle$ can also be coarse-grained as a wave function. This process, termed *wave-function renormalization* in Ref. 111, is thoroughly equivalent to *entanglement renormalization*^{29,33} and produces a MERA²⁹ as a result. Therefore, the exact transformation W_{exact} discussed in this article can also be used in the context of wave-function renormalization.

B. Conclusions

Tensor network algorithms offer a variational approach to strongly interacting systems on a lattice that is free of the sign problem and can therefore be applied to systems that are beyond the reach of Monte Carlo sampling techniques, such as frustrated antiferromagnets and interacting fermions. In this article we have explored the use of tensor network

techniques in the context of lattice gauge theory and, more broadly, systems with topological order. We have explain how to incorporate a local symmetry into a coarse-graining scheme and the resulting variational ansatz for the simplest nontrivial case of the Z_2 lattice gauge theory.

We envisage that proper generalizations of the results presented here, possibly along the lines of those discussed in Sec. VII A, will constitute the basis for future numerical simulations of lattice gauge theories and more general models with topological order.

ACKNOWLEDGMENTS

We thank M. Aguado, P. Calabrese, P. Corboz, A. Di Giacomo, M. D’Elia, G. Evenbly, F. Gliozzi, A. Hamma, J. I. Latorre, and G. Sierra for useful discussions and comments. The authors acknowledge financial support from the Australian Research Council (FF0668731, DP0878830, DP1092513).

APPENDIX A: DUALITY TRANSFORMATION

In this appendix we review the well-known duality transformation^{40,42} between Z_2 lattice gauge theory and the quantum Ising model in two spatial dimensions as described in Sec. III D; see Fig. 8. The transformation is expressed in terms of CNOT gates in order to highlight its similarities and differences with the analytical transformation W_{exact} used in this work.

As indicated in Figs. 40–44 for the case of a lattice of 4×4 sites with periodic boundary conditions in both directions, this transformation can be implemented as a sequence of CNOT

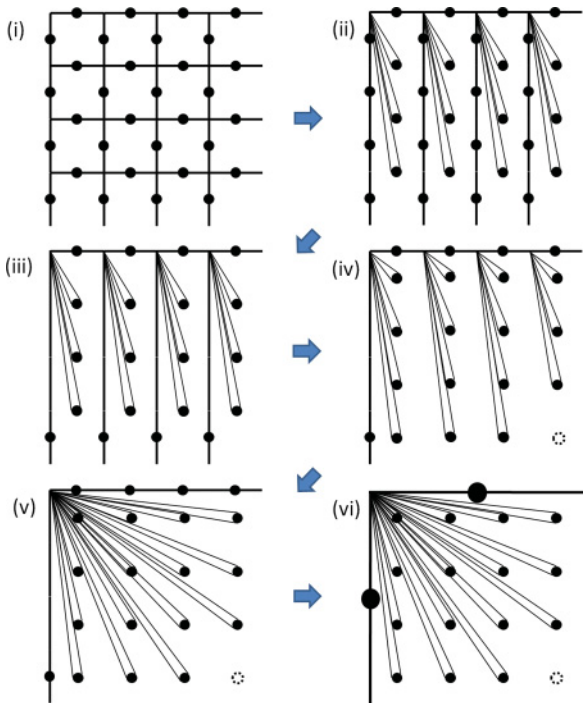


FIG. 40. (Color online) Duality transformation between the Z_2 lattice gauge theory and the quantum Ising model, broken into six stages [(i)–(vi)].

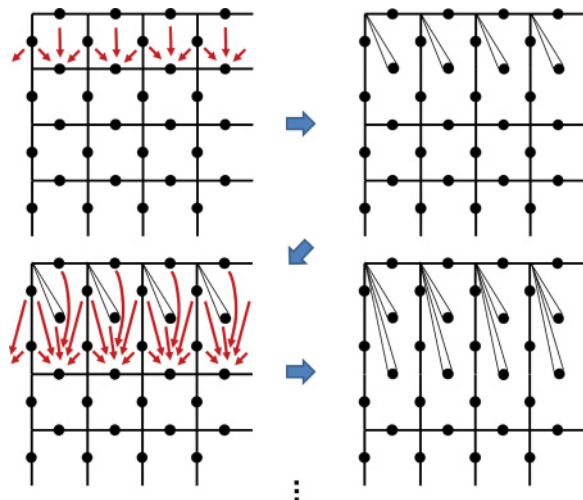


FIG. 41. (Color online) CNOT gates that transform stage (i) into stage (ii). The sequence proceeds from top to bottom. Only two of the three required steps are depicted. In a $L \times L$ lattice, $L - 1$ such steps are required.

gates as indicated. Figure 40 represents six stages [(i)–(vi)] of this transformation, with stages (i) and (vi) corresponding to the Z_2 lattice gauge theory and the quantum Ising model, respectively.

Figure 41 indicates the sequence of CNOT gates that transform stage (i) into stage (ii). This sequence progresses from top to bottom and can be divided into four columns of CNOT gates, where gates in different columns commute. Figure 42 indicates the sequence of CNOT gates that transform stage (ii) into stage (iii). Again, the sequence progresses from top to bottom and can be divided into four columns of CNOTs gates, where gates in different columns commute. Figure 43 explains how to transform stage (iii) into stage (iv). Note that stages (iv) and (v) are equivalent, since they differ only in where the single-spin plaquettes are connected to the rest

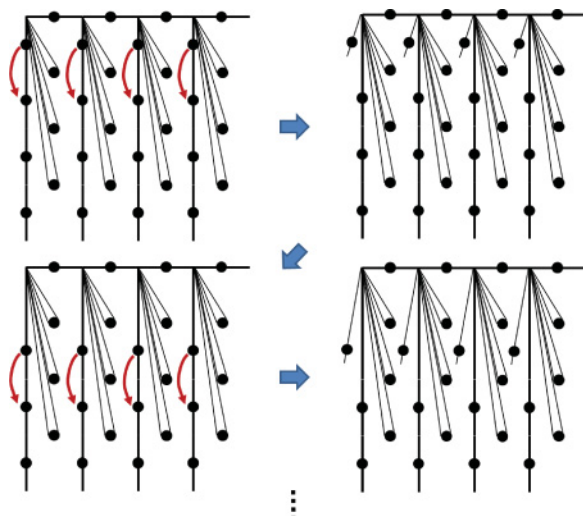


FIG. 42. (Color online) CNOT gates that transform stage (ii) into stage (iii). The sequence proceeds from top to bottom. Only two of the three required steps are depicted. In a $L \times L$ lattice, $L - 1$ such steps are required.

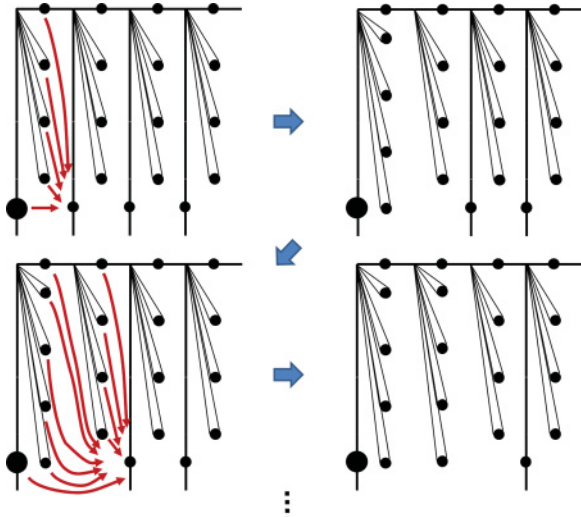


FIG. 43. (Color online) CNOT gates that transform stage (iii) into stage (iv). Note that stage (iii) contains four columns of single-spin plaquettes, with three spins on each column. Instead, stage (iv) contains four columns of single-spin plaquettes with four spins on each column, except for the rightmost column, which only contains three spins and a vacancy. The sequence proceeds from left to right. Only two of the three required steps are depicted. In a $L \times L$ lattice, $L - 1$ such steps are required.

of the lattice; that is, they correspond exactly to the same Hamiltonian. Finally, Fig. 44 shows how to transform stage (v) into stage (vi), corresponding to the Ising model.

APPENDIX B: ASSESSMENT OF THE PRECISION OF THE NUMERICAL RESULTS

Section VI presented a number of numerical results for the deformed toric code Hamiltonian H_{TC}^x on a torus of linear size $L = 4, 6,$ and 8 , obtained with a hybrid tensor network with a fixed value of the refinement parameter $\chi = 100$. Those results successfully reproduced both quantitatively and qualitatively

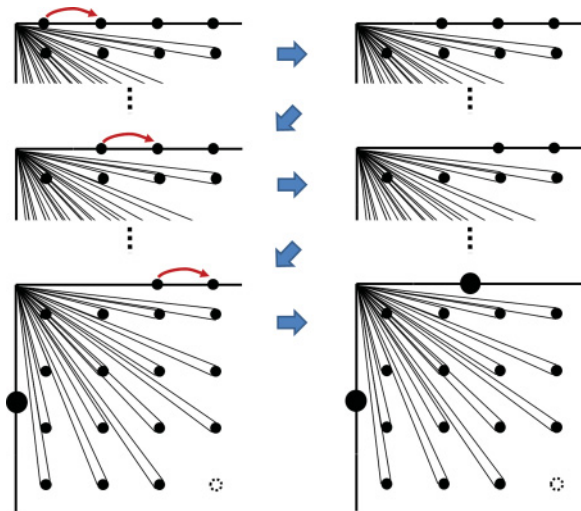


FIG. 44. (Color online) CNOT gates that transform stage (v) into stage (vi). Three required steps are depicted. In a $L \times L$ lattice, $L - 1$ such steps are required.

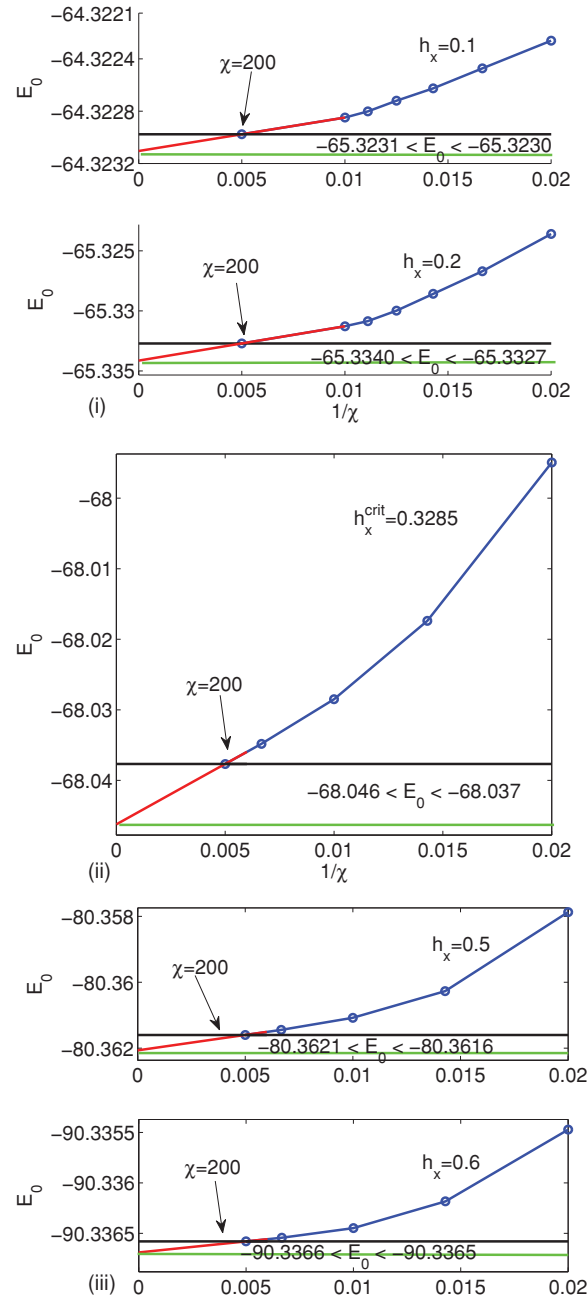


FIG. 45. (Color online) Ground-state energy E_0 for the deformed toric code on a 8×8 torus as a function of the refinement parameter $1/\chi$ for different values of the magnetic field, (i) $h_x = 0.1$ and $h_x = 0.2$ in the topological phase, (ii) $h_x^{crit} = 0.3285$ at the critical point, and (iii) $h_x = 0.5$ and $h_x = 0.6$ in the spin-polarized phase. Results of the simulations in the range of refinement parameter $50 \leq \chi \leq 200$ are shown with blue circles. We estimate upper and lower bounds for the ground-state energy using the analysis of Ref. 78. The upper bound indicated by a black horizontal line is the value of E_0 at $\chi = 200$ while the lower bound is shown by a green line. In the plots we also write the exact numerical values for both upper and lower bounds. They provide narrow windows (in general around 0.01% or less of the exact value) in which the exact ground-state energy is contained.

the main properties of the ground state of the system in the deconfined and spin-polarized phases and of the second-order phase transition between them. In this appendix we perform a

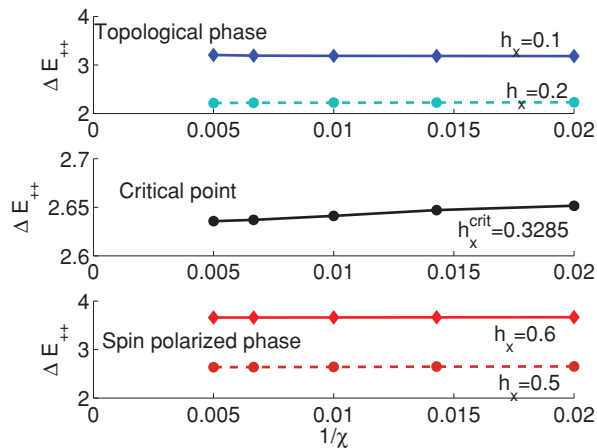


FIG. 46. (Color online) Scaling of the gap ΔE_{++} for the deformed toric code on the 8×8 torus as a function of $1/\chi$ for different values of the magnetic field in the topological phase, $h_x = 0.1$ and $h_x = 0.2$ (top), at the critical point, $h_x^{\text{crit}} = 0.3285$ (middle), and in the spin-polarized phase, $h_x = 0.5$ and $h_x = 0.6$ (bottom). The dependence of the gap as a function of $1/\chi$ is not uniform as in the case of the ground-state energy and thus we cannot extract rigid bounds on its value. However, due to the small variations of the gap as a function of χ in the range $50 \leq \chi \leq 200$ (in the worst case of the critical point of about 1% of its value) compared with its large variation as a function of the magnetic field h_x , we can neglect the dependence on χ of the gap provided we accept an uncertainty of about 1% on the actual gap value.

scaling analysis with respect to χ to show that the particular choice $\chi = 100$ used in Sec. VI did not have a significant effects on the numerical results.

We start by reminding that the hybrid tensor network ansatz is, as far as its numerical part W_{num} is concerned, a tree tensor network TTN, namely one used to approximate the ground state of the lattice model after being transformed according to W_{exact} . As discussed in Ref. 78, a sufficiently large value of χ will reproduce the ground state to arbitrary accuracy, but this value will have to be exponentially large in the linear size L of the lattice.

Our scaling analysis consists of two parts. First we study, in a torus of linear size $L = 8$, the convergence of the ground-state energy as a function of $1/\chi$, see Fig. 45, for specific values of the magnetic field h_x , namely $h_x = \{0.1, 0.2\}$ (deconfined phase), $h_x = \{0.5, 0.6\}$ (spin-polarized phase), and $h = 0.33 \approx h_x^{\text{crit}}$ (critical point). From these results, lower and upper bounds to the ground-state energy are obtained by observing that the ground-state energy is a monotonic function of $1/\chi$, $E_0(1/\chi)$, with positive, monotonically increasing derivative.⁷⁸ Assuming that this trend continues all the way to $1/\chi = 0$, this implies that $E_0(\chi = 200)$ provides us with the best upper bound to the ground-state energy, while a lower bound can be found with a linear extrapolation of $E_0(\chi = 150)$ and $E_0(\chi = 200)$ (the two best results) to $1/\chi = 0$. For all

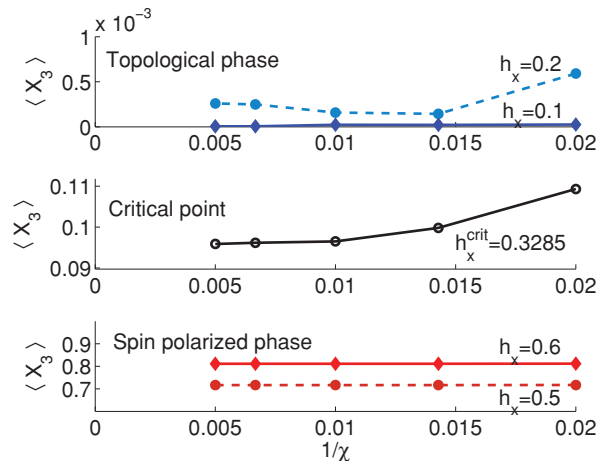


FIG. 47. (Color online) Scaling of the disorder parameter $\langle X_3 \rangle$ for the deformed toric code on the 8×8 torus as a function of $1/\chi$ for different values of the magnetic field in the topological phase, $h_x = 0.1$ and $h_x = 0.2$ (top), at the critical point, $h_x^{\text{crit}} = 0.3285$ (middle), and in the spin polarized phase, $h_x = 0.5$ and $h_x = 0.6$ (bottom). On the one hand, the values in the deconfined phase (top) are compatible with the theoretical expectation that the disorder parameter vanishes. However, they fluctuate substantially as a function of χ (we appreciate variations of around 30% around the value of disorder parameter at $h_x = 0.2$). We can still distinguish the results at $h_x = 0.1$, where the disorder parameter fluctuates around 10^{-5} , from those at $h_x = 0.2$ where it fluctuates around 10^{-4} . We believe that the origin of these large fluctuations is due not as much to the finite size of χ as to a lack of convergence of the iterative procedure used to compute the ground state, combined with the small values of the disordered parameter. Our iterative optimization procedure is stopped when the ground-state energy has converged to about 10 digits. This criterion could be insufficient for a disorder parameter if the relevant critical exponents imply a much slower convergence than the ground-state energy.¹¹² On the other hand, both at the critical point (central panel) and in the spin-polarized phase (lower panel), we extract again very accurate results and we can neglect the dependence on χ of the disorder parameter by introducing a systematic error lower than 1% of its actual value.

the values of the magnetic field considered these bounds provide narrow windows (around 0.01% of the actual value).

Once we have established the level of convergence of the ground-state energy, we look at the dependence of other observables with χ . Figures 46 and 47 show the disorder parameter $\langle X_3 \rangle$ and the gap $\Delta E_{(+,+)}$ in the $(+, +)$ sector, respectively. In contrast with the ground-state energy, which was monotonic in $1/\chi$, we see that $\langle X_3 \rangle$ and $\Delta E_{(+,+)}$ behave more erratically as a function of $1/\chi$. In this case, we can use the variations in value as a function of $1/\chi$ as an estimate of the error introduced by finite χ . Importantly, this error is much smaller than the variation of $\langle X_3 \rangle$ and $\Delta E_{(+,+)}$ as a function of the magnetic field h_x . Further description is left to the captions of the figures.

¹C. W. Misner, K. S. Thorne, and J. A. Wheeler, *Gravitation* (W. H. Freeman, San Francisco, 1973).

²M. E. Peskin and D. V. Schroeder, *An Introduction to Quantum Field Theory* (Addison-Wesley, Boston, 1995).

³K. G. Wilson, *Phys. Rev. D* **10**, 2445 (1974).

⁴G. S. Bali, *Phys. Rept.* **343**, 1 (2001).

⁵H. Fukaya, S. Aoki, S. Hashimoto, T. Kaneko, J. Noaki, T. Onogi, and N. Yamada, *Phys. Rev. Lett.* **104**, 122002 (2010).

- ⁶A. Bazavov, C. Bernard, C. DeTar, S. Gottlieb, U. M. Heller, J. E. Hetrick, J. Laiho, L. Levkova, P. B. Mackenzie, M. B. Oktay, R. Sugar, D. Toussaint, and R. S. V. de Water, *Rev. Mod. Phys.* **82**, 1349 (2010).
- ⁷S. B. Ruster, V. Werth, M. Buballa, I. A. Shovkovy, and D. H. Rischke, *Phys. Rev. D* **72**, 034004 (2005).
- ⁸I. Affleck, T. Kennedy, E. H. Lieb, and H. Tasaki, *Commun. Math. Phys.* **115**, 477 (1988).
- ⁹M. Fannes, B. Nachtergaele, and R. F. Werner, *Commun. Math. Phys.* **144**, 443 (1992).
- ¹⁰S. Östlund and S. Rommer, *Phys. Rev. Lett.* **75**, 3537 (1995).
- ¹¹S. R. White, *Phys. Rev. Lett.* **69**, 2863 (1992).
- ¹²S. R. White, *Phys. Rev. B* **48**, 10345 (1993).
- ¹³U. Schollwöck, *Rev. Mod. Phys.* **77**, 259 (2005).
- ¹⁴F. Verstraete and J. I. Cirac, e-print [arXiv:cond-mat/0407066v1](https://arxiv.org/abs/cond-mat/0407066v1) (2004).
- ¹⁵J. Jordan, R. Orús, G. Vidal, F. Verstraete, and J. I. Cirac, *Phys. Rev. Lett.* **101**, 250602 (2008).
- ¹⁶F. Verstraete, V. Murg, and J. I. Cirac, *Adv. Phys.* **57**, 143 (2008).
- ¹⁷Z.-C. Gu, M. Levin, and X.-G. Wen, *Phys. Rev. B* **78**, 205116 (2008).
- ¹⁸Z.-C. Gu and X.-G. Wen, *Phys. Rev. B* **80**, 155131 (2009).
- ¹⁹V. Murg, F. Verstraete, and J. I. Cirac, *Phys. Rev. B* **79**, 195119 (2009).
- ²⁰Z. Y. Xie, H. C. Jiang, Q. N. Chen, Z. Y. Weng, and T. Xiang, *Phys. Rev. Lett.* **103**, 160601 (2009).
- ²¹P. Chen, C.-Y. Lai, and M.-F. Yang, *J. Stat. Mech.: Theor. Exp.* **2009**, P10001 (2009).
- ²²H. H. Zhao, Z. Y. Xie, Q. N. Chen, Z. C. Wei, J. W. Cai, and T. Xiang, *Phys. Rev. B* **81**, 174411 (2010).
- ²³C. V. Kraus, N. Schuch, F. Verstraete, and J. I. Cirac, *Phys. Rev. A* **81**, 052338 (2010).
- ²⁴P. Corboz, R. Orús, B. Bauer, and G. Vidal, *Phys. Rev. B* **81**, 165104 (2010).
- ²⁵T. Barthel, C. Pineda, and J. Eisert, *Phys. Rev. A* **80**, 042333 (2009).
- ²⁶G. Sierra and M. A. Martin-Delgado, e-print [arXiv:cond-mat/9811170](https://arxiv.org/abs/cond-mat/9811170) (1998).
- ²⁷N. Maeshima, Y. Hieida, Y. Akutsu, T. Nishino, and K. Okunishi, *Phys. Rev. E* **64**, 016705 (2001).
- ²⁸Y. Nishio, N. Maeshima, A. Gendiar, and T. Nishino, e-print [arXiv:cond-mat/0401115](https://arxiv.org/abs/cond-mat/0401115) (2004).
- ²⁹G. Vidal, *Phys. Rev. Lett.* **99**, 220405 (2007).
- ³⁰G. Vidal, *Phys. Rev. Lett.* **101**, 110501 (2008).
- ³¹L. Cincio, J. Dziarmaga, and M. M. Rams, *Phys. Rev. Lett.* **100**, 240603 (2008).
- ³²G. Evenbly and G. Vidal, *Phys. Rev. Lett.* **102**, 180406 (2009).
- ³³G. Evenbly and G. Vidal, *Phys. Rev. B* **79**, 144108 (2009).
- ³⁴V. Giovannetti, S. Montangero, M. Rizzi, and R. Fazio, *Phys. Rev. A* **79**, 052314 (2009).
- ³⁵G. Evenbly and G. Vidal, *Phys. Rev. Lett.* **104**, 187203 (2010).
- ³⁶P. Corboz and G. Vidal, *Phys. Rev. B* **80**, 165129 (2009).
- ³⁷C. Pineda, T. Barthel, and J. Eisert, *Phys. Rev. A* **81**, 50303 (2010).
- ³⁸F. Mezzacapo and J. I. Cirac, *New J. Phys.* **12**, 103039 (2010).
- ³⁹S.-H. Li, Q.-Q. Shi, and H.-Q. Zhou, e-print [arXiv:1001.3343v1](https://arxiv.org/abs/1001.3343v1) (2010).
- ⁴⁰F. Wegner, *J. Math. Phys.* **12**, 2259 (1971).
- ⁴¹D. Horn, M. Weinstein, and S. Yankielowicz, *Phys. Rev. D* **19**, 3715 (1979).
- ⁴²J. B. Kogut, *Rev. Mod. Phys.* **51**, 659 (1979).
- ⁴³X. Wen, *Adv. Phys.* **44**, 405 (1995).
- ⁴⁴A. Y. Kitaev, *Ann. Phys.* **303**, 2 (2003).
- ⁴⁵N. Read and S. Sachdev, *Phys. Rev. Lett.* **66**, 1773 (1991).
- ⁴⁶X. G. Wen, *Phys. Rev. B* **44**, 2664 (1991).
- ⁴⁷N. Read and S. Sachdev, *Int. J. Mod. Phys. B* **5**, 219 (1991).
- ⁴⁸S. Sachdev, Lectures at the Les Houches School on “Modern theories of correlated electron systems,” France, May 2009 (2009), e-print [arXiv:1002.3823v2](https://arxiv.org/abs/1002.3823v2).
- ⁴⁹S. Trebst, P. Werner, M. Troyer, K. Shtengel, and C. Nayak, *Phys. Rev. Lett.* **98**, 070602 (2007).
- ⁵⁰A. Hamma and D. A. Lidar, *Phys. Rev. Lett.* **100**, 030502 (2008).
- ⁵¹T. Sugihara, *J. High Energy Phys.* **2005**, 022 (2005).
- ⁵²N. Schuch, I. Cirac, and D. Perez-Garcia, e-print [arXiv:1001.3807v2](https://arxiv.org/abs/1001.3807v2) (2010).
- ⁵³B. Swingle and X.-G. Wen, e-print [arXiv:1001.4517v1](https://arxiv.org/abs/1001.4517v1) (2010).
- ⁵⁴X. Chen, B. Zeng, Z.-C. Gu, I. L. Chuang, X.-G. Wen, *Phys. Rev. B* **82**, 165119 (2010).
- ⁵⁵C. J. Hamer, *J. Phys. A: Math. Gen.* **33**, 6683 (2000).
- ⁵⁶I. P. McCulloch and M. Gulacsi, *Europhys. Lett.* **57**, 852 (2002).
- ⁵⁷G. Sierra and T. Nishino, *Nucl. Phys. B* **495**, 505 (1997).
- ⁵⁸P. Buividovich and M. Polikarpov, *Phys. Lett. B* **670**, 141 (2008).
- ⁵⁹L. P. Kadanoff and H. Ceva, *Phys. Rev. B* **3**, 3918 (1971).
- ⁶⁰J. Frohlich and P. A. Marchetti, *Commun. Math. Phys.* **112**, 343 (1987).
- ⁶¹L. D. D. A. Di Giacomo and G. Paffuti, *Phys. Lett. B* **349**, 513 (1995).
- ⁶²I. Montvay and G. Munster, *Cambridge Monographs on Mathematical Physics* (Cambridge University Press, Cambridge, UK, 1994), Vol. 491.
- ⁶³J. B. Kogut and L. Susskind, *Phys. Rev. D* **11**, 395 (1975).
- ⁶⁴J. B. Kogut, *Phys. Rept.* **67**, 67 (1980).
- ⁶⁵G. Marchesini and E. Onofri, *Nuovo Cimento A* **65**, 298 (1981).
- ⁶⁶E. Fradkin and S. H. Shenker, *Phys. Rev. D* **19**, 3682 (1979).
- ⁶⁷G. Bhanot and M. Creutz, *Phys. Rev. D* **21**, 2892 (1980).
- ⁶⁸V. Agostini, G. Carlino, M. Caselle, and M. Hasenbusch, *Nucl. Phys. B* **484**, 331 (1997).
- ⁶⁹R. Savit, *Rev. Mod. Phys.* **52**, 453 (1980).
- ⁷⁰E. Cobanera, G. Ortiz, and Z. Nussinov, *Phys. Rev. Lett.* **104**, 020402 (2010).
- ⁷¹B. Svetitsky and L. G. Yaffe, *Nucl. Phys. B* **210**, 423 (1982).
- ⁷²E. Fradkin and L. Susskind, *Phys. Rev. D* **17**, 2637 (1978).
- ⁷³D. Gottesman, Ph.D. thesis, Caltech, 1997.
- ⁷⁴E. Dennis, A. Kitaev, A. Landahl, and J. Preskill, *J. Math. Phys.* **43**, 4452 (2002).
- ⁷⁵H. X. He, C. J. Hamer, and J. Oitmaa, *J. Phys. A: Math. Gen.* **23**, 1775 (1990).
- ⁷⁶J. Oitmaa, C. J. Hamer, and Z. Weihong, *J. Phys. A: Math. Gen.* **24**, 2863 (1991).
- ⁷⁷A. Pelissetto and E. Vicari, *Phys. Rep.* **368**, 549 (2002).
- ⁷⁸L. Tagliacozzo, G. Evenbly, and G. Vidal, *Phys. Rev. B* **80**, 235127 (2009).
- ⁷⁹G. Vidal, in *Understanding Quantum Phase Transitions*, edited by Lincoln D. Carr (Colorado School of Mines, Golden, USA, 2010).
- ⁸⁰K. G. Wilson, *Rev. Mod. Phys.* **55**, 583 (1983).
- ⁸¹V. Giovannetti, S. Montangero, and R. Fazio, *Phys. Rev. Lett.* **101**, 180503 (2008).
- ⁸²R. N. C. Pfeifer, G. Evenbly, and G. Vidal, *Phys. Rev. A* **79**, 040301 (2009).
- ⁸³M. Aguado and G. Vidal, *Phys. Rev. Lett.* **100**, 070404 (2008).

- ⁸⁴R. König, B. W. Reichardt, and G. Vidal, *Phys. Rev. B* **79**, 195123 (2009).
- ⁸⁵S. Singh, R. N. C. Pfeifer, and G. Vidal, *Phys. Rev. A* **82**, 050301 (2010).
- ⁸⁶E. Fradkin and S. Raby, *Phys. Rev. D* **20**, 2566 (1979).
- ⁸⁷A. A. Migdal, *ZhETF* **69**, 810 (1975) [*Sov. Phys. JETP* **42**, 413 (1975)].
- ⁸⁸M. A. Levin and X.-G. Wen, *Phys. Rev. B* **71**, 45110 (2005).
- ⁸⁹M. B. Green, *Nucl. Phys. B* **144**, 0473 (1978).
- ⁹⁰E. Rico (private communication).
- ⁹¹G. 't Hooft, *Nucl. Phys. B* **190**, 455 (1981).
- ⁹²S. Mandelstam, *Phys. Rept.* **23**, 245 (1976).
- ⁹³L. Tagliacozzo and G. Vidal, in preparation (2010).
- ⁹⁴M. P. Nightingale, *Physica A* **83**, 561 (1975).
- ⁹⁵M. D'Elia and L. Tagliacozzo, *Phys. Rev. D* **74**, 114510 (2006).
- ⁹⁶P. Zanardi and N. Paunković, *Phys. Rev. E* **74**, 031123 (2006).
- ⁹⁷J.-H. Liu, Q.-Q. Shi, H.-L. Wang, J. Links, and H.-Q. Zhou, e-print [arXiv:0909.3031](https://arxiv.org/abs/0909.3031) (2009).
- ⁹⁸M. Cozzini, P. Giorda, and P. Zanardi, *Phys. Rev. B* **75**, 014439 (2007).
- ⁹⁹M. Cozzini, R. Ionicioiu, and P. Zanardi, *Phys. Rev. B* **76**, 104420 (2007).
- ¹⁰⁰L. Campos Venuti and P. Zanardi, *Phys. Rev. Lett.* **99**, 095701 (2007).
- ¹⁰¹P. Buonsante and A. Vezzani, *Phys. Rev. Lett.* **98**, 110601 (2007).
- ¹⁰²W.-L. You, Y.-W. Li, and S.-J. Gu, *Phys. Rev. E* **76**, 022101 (2007).
- ¹⁰³S.-J. Gu, H.-M. Kwok, W.-Q. Ning, and H.-Q. Lin, *Phys. Rev. B* **77**, 245109 (2008).
- ¹⁰⁴H.-Q. Zhou, R. Orús, and G. Vidal, *Phys. Rev. Lett.* **100**, 080601 (2008).
- ¹⁰⁵I. S. Tupitsyn, A. Kitaev, N. V. Prokof'ev, and P. C. E. Stamp, *Phys. Rev. B* **82**, 085114 (2010).
- ¹⁰⁶S. Bravyi, M. Hastings, and S. Michalakis, *J. Math. Phys.* **51**, 093512 (2010).
- ¹⁰⁷J. Vidal, S. Dusuel, and K. P. Schmidt, *Phys. Rev. B* **79**, 033109 (2009).
- ¹⁰⁸J. Vidal, R. Thomale, K. P. Schmidt, and S. Dusuel, *Phys. Rev. B* **80**, 081104 (2009).
- ¹⁰⁹T. Nishino and K. Okunishi, *J. Phys. Soc. Jpn.* **65**, 891 (1996).
- ¹¹⁰R. Orús and G. Vidal, *Phys. Rev. B* **80**, 094403 (2009).
- ¹¹¹X. Chen, Z.-C. Gu, and X.-G. Wen, *Phys. Rev. B* **82**, 155138 (2010).
- ¹¹²C. Liu, L. Wang, A. W. Sandvik, Y.-C. Su, and Y.-J. Kao, *Phys. Rev. B* **82**, 060410 (2010).